Electrolyte Property Influences on Hydrodynamic and Morphological Stability in Metal Batteries

A Dissertation

Presented to the Faculty of the Graduate School

of Cornell University

In Partial Fulfillment of the Requirements for the Degree of

Doctor of Philosophy

by

Alexander James Warren

August 2020

Electrolyte Property Influences on Hydrodynamic and Morphological Stability in Metal Batteries

Alexander James Warren, Ph. D.

Cornell University 2020

As the energy supply shifts from fossil fuels to inherently intermittent renewable energy sources, such as wind and solar, improvements in energy storage are required. Electrical energy storage in the form of rechargeable batteries can benefit greatly from a transition to energy dense metallic anodes that require safe, reversible, electrodeposition over many cycles of charge and discharge. In all currently used electrolytes, electrodeposition is subject to three types of instabilities: chemical, morphological, and hydrodynamic at both low and high current densities, which lead to complex transport phenomena in the electrolyte and unstable deposition, including formation of ramified structures known as dendrites. We focus on understanding the hydrodynamic instability termed electroconvection. We have developed viscoelastic liquid electrolytes to stabilize electroconvective instabilities near the electrode and improve deposit morphology. These designs consist of high molecular weight polymers that are entangled in common battery electrolytes. A key aspect of these electrolytes is the decoupling of ion and momentum transport, in which the viscosity is significantly enhanced while maintaining high ionic conductivities. These electrolytes have been studied with a metallic electrode that is subject to morphological changes, and at a more

fundamental level, using ion selective membranes to isolate the hydrodynamic instability. Through these techniques the convection was found to be arrested when the polymer is present above its entanglement transition. This was further confirmed through in-situ visualization coupled with particle tracking in which the polymer significantly stabilized the motion near the ion-selective interface. The visualization was expanded to understand the convective flow structure under a variety of applied potentials and electrolyte concentrations. Through our particle tracking it has been found that electroconvection occurs on multiple length scales simultaneously. It was discovered that increases in applied potential both enhance the velocity and complexity of the convective motions. Beyond this, decreases in concentration, accompanied by larger Debye screening lengths, enhance chaos in the flow and impact the ratio of small to large convective motions in the electrolyte.

BIOGRAPHICAL SKETCH

Alex Warren received his B.S in Chemical Engineering from Case Western Reserve University in 2016. He then received his Ph.D. in Chemical Engineering from Cornell University in 2020 under the supervision of Dr. Lynden Archer. His research focuses on the impacts of electrolyte properties on hydrodynamic and morphological instabilities in metal electrodeposition.

Dedicated to my family and all those who have supported me

ACKNOWLEDGMENTS

I would like to express my gratitude for all those who have assisted me in my life and academic journey. Firstly, I would like to thank my supervisor Professor Lynden Archer for the tremendous amount of help and guidance he has provided me in my Ph.D. studies. Throughout my time at Cornell, Dr. Archer was able to stretch my curiosity and enjoyment of scientific research well beyond what I could do alone. His knowledge and enthusiasm for a wide array of subjects pushed me to become a better researcher and a better person overall. I would also like to thank my committee members Professor Don Koch and Professor Robert Shepherd for the research discussions and assistance they have provided.

I would also like to thank the current and former Archer Research group members that I have had the pleasure of working alongside. The numerous discussions and assistance we have shared, as well as the collaborative spirit has helped me immensely. Thank you to all of my friends who have supported me in my academic interests and goals outside of Cornell.

Finally, I want to recognize my family for all their support throughout my life. The encouragement I have received from my parents and sister has been crucial to everything I have been able to accomplish. Without them I would not have become the person I am today.

TABLE OF CONTENTS

LIST OF FIGURES

Chapter 1: Introduction

1.1 Cost Effective Storage of Electrical Energy

Substantial reductions in greenhouse gas emissions, including carbon dioxide, are required to limit the harmful effects of global climate change. Renewable energy sources, such as wind and solar photovoltaics, are compelling technologies to reduce the carbon footprint associated with electricity generation. They have even begun to rival fossil fuel derived energy on price per kWh [1]. However, these energy sources are intermittent in nature making energy storage a necessity to transition our electricity supply to these types of renewables [2]. Additionally, electricity generation accounts for only 27% of our greenhouse gas emissions while transportation accounts for 28% of the emissions in the United States [3]. Therefore, electrifying transportation and enabling renewables with an electrical energy storage device, such as an energy dense battery, can have a crucial impact on humanity's carbon emissions.

Recent growth in the commercial battery market is overwhelmingly dominated by lithium ion batteries. As materials advances in the anode, electrolyte, and cathodes pushes this technology towards its theoretical capacity and charging speed limits, safety concerns have intensified as manufacturers strive to achieve incremental performance improvements. Consumers have been put in danger from short circuiting and thermal runaway that lead to fires and explosions in these cells. Therefore, a new technology is needed for continued improvements in the specific energy density and capacity of electrical energy storage devices [4,5]. One intriguing possibility is a family of devices that utilize a metallic anode instead of the graphitic host used in the lithium ion battery

[5-8]. Instead of intercalating into the anodic host material, the metal cations are directly plated onto the anode; storing electrical energy in their reduced form. This simplicity comes with the benefit of increased energy density; a rechargeable lithium metal battery theoretically has 2-4 times the energy density of a lithium ion battery when paired with an energy dense cathode material [6]. However, metal batteries come with a host of issues that have limited their marketability up to this point. The main problem shared by most technologies in this class come from the uneven deposition of the metal causing non-planar deposits on planar substrates that, depending on the metal and deposition conditions, may exhibit, whisker-like, moss-like, or fractal dendrite-like morphologies [5]. Non-planar structures in any of these morphologies, loosely termed *dendrites*, will overtime proliferate in the inter-electrode space inside a battery, which can pierce the battery separator and cause a short circuit between the two electrodes. With flammable electrolytes dominating this space, short circuits create a major safety concern. Another difficult problem is apparent when using a reactive metal, such as lithium or sodium, in which there is a continued reaction between the metal and the electrolyte components [5-7]. This reaction depletes the electrolyte and reduces the coulombic efficiency of the battery, causing its ability to store electric energy to deteriorate over time. The two processes often work synergistically — uneven deposition results in more surface area for the reaction, further depleting the solvent and salts, driving rapid failure of the battery.

Rechargeable metal batteries encompass a wide array of chemistries that could see potential uses in the commercial market. The subset of metallic anodes attracting the greatest interest are Zn [8,9], Al [10,11], Li [5-7], and Na [12]. Zinc and Aluminum

are good prospects because of the low cost, material abundance, and compatibility of these metals with aqueous electrolytes. Sodium and lithium are widely studied because of the high theoretical energy densities when these metals are paired with a high capacity cathode such as Sulfur or Oxygen. While the basics of the electrochemistry rely on metal cations being reduced onto the anode, the origins of rough deposition in reactive (Na, Li) and non-reactive (Zn, Al) metals are vastly different.

For reactive metals, a well-known problem begins when the metal electrode comes into contact with the electrolyte. The highly negative electrochemical potential at which the metal is reduced (*e.g.*, $Li^+ \rightarrow Li$) in the storage reaction, place all components of the electrolyte outside of their electrochemical stability limits, causing immediate and complex reactions of the solvent and salt of the electrolyte in tandem with the metal reduction process [5,6,13]. The byproducts of these reactions yield a passivation layer on the metal surface known as the solid electrolyte interphase or SEI. Because this process is typically spontaneous and uncontrolled, an inhomogeneous SEI forms resulting in a heterogeneous distribution of high conduction pathways for cations to reach the electrode. Nucleates are formed at these spaces and their growth results in a rough mossy deposit [5].

For the non-reactive metals, dendrites are predicted to occur under conditions where the battery recharge operation approaches the transport limit of the electrolyte [14-16]. Specifically, for every electrolyte there is a maximum rate of diffusion of the ions within the system. As the current/rate of recharge is pushed towards higher values, this limiting current is approached and loss of the ions nearest the electrode as a result of the electrochemical reduction reaction cannot be fully replenished by simple

diffusion from the bulk. This creates a situation in which there is a boundary layer of depleted ions, known as the diffusion boundary layer [17,18]. Operated under these conditions, protruding features (*e.g.*, caused by roughness) of the metal electrode can access more of the limited supply of ions and will grow at a faster rate relative to its flat surroundings. Convection, as a result of depleted ions, can also transport ions preferentially to these growing deposits [19-21]. As this process propagates further into the diffusion layer the electric field lines concentrate to the tip and ions will preferentially deposit onto the dendrite. These types of dendrites grow from the tip and typically manifest as sharp tree-like structures. These structures can be seen in figure 1a,b for deposition of copper and zinc.

Interestingly, it has been reported by Bai et al. that when the operation of a reactive metal anode is pushed to its diffusion limitations the unstable growth becomes similar to that of the non-reactive metals [22]. This growth transition can be seen in figure 1c. With similar effects for most metal deposition found under diffusional limitations, we focus on reducing dendrite propagation within this high current regime. Within this focus, the ion motion becomes more complex as new forms of transport, such as hydrodynamic instabilities, impact the deposition morphology.

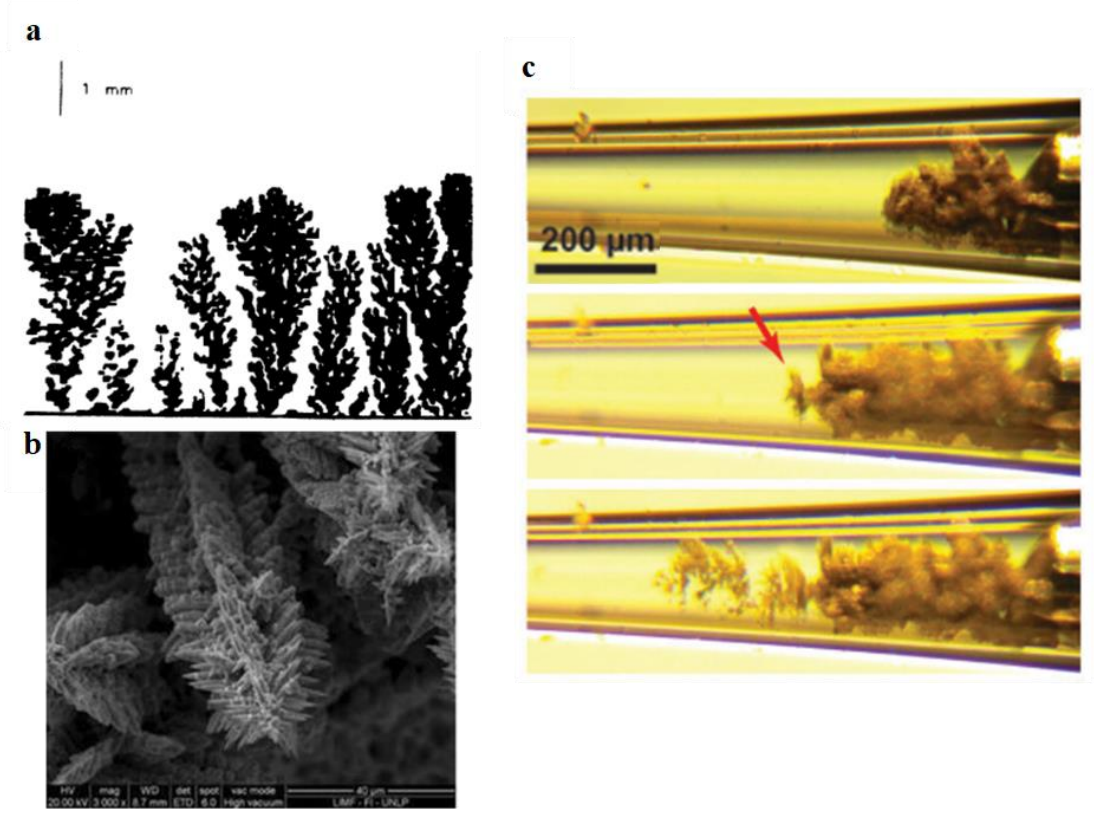

Figure 1: **a)** Growth patterns of electrodeposited Copper from 0.05M $CuSO_{4\,(aq)}$ at a polarization of -5.0V for approximately 8-10 minutes [23]. **b)** SEM image of dendrites at the edge of zinc plated washers at 600mA/cm^2 [24]. **c)** Transition from mossy lithium deposition to tip growing dendrites under diffusional limitations [22]

1.2 Hydrodynamic Instabilities

At ion-selective interfaces the current is traditionally thought to be limited by the maximum rate of diffusion of ions to the surface [17]. This diffusion limited current is given in equation 1, where J_{lim} is the limiting current density, z is the valency of the cation, F is Faraday's Constant, D is the diffusivity, L is the interelectrode spacing, t_c is the transference number of the cation and $C_b$is the concentration of the electroactive species in the bulk.

$$J_{lim} = \frac{2z_C FD}{(1-t_{C)}L} C_b \quad (1)$$

The ion selective surfaces at which these physics may occur extend well beyond those of interest for energy storage. They include cation (or anion) selective membranes used in desalination [25,26] and dialysis [27] or the selective surface may be a metal electrode, used for electroplating [19,20] or an energy dense metal battery [5]. Based on a limiting solution of the Nernst-Plank equations, conventional thinking is that the limiting current would be maintained until the electrolyte is pushed beyond its voltage stability limits. However, at large polarizations, ion transport rates well above the diffusion limit (*overlimiting conduction*) were demonstrated in experiments performed decades ago [28-30]. As the current surpasses the diffusion limit, the experiments also report an increase in electric noise. These behaviors were first explained to be an additional current resulting from the breakdown of the electrolyte solvent, namely the dissociation of the water [29,31,32]. Another proposed explanation was the influence of gravity on the electrolyte enhancing the transport [33]. However, these early explanations have been progressively ruled out as more sophisticated analyses of results from old and new experiments have been performed [34,35]. Rubinstein and coworkers proposed a theoretical explanation that convective motions enhanced the transport, yielding the overlimiting current seen in experiments [35-37]. In a simple, but clever experiment, this explanation was verified by showing that the overlimiting conductance and noise can both be shut down at high polarizations by immobilizing the electrolyte near an ion-selective interface using a gel coating [38]. The generally accepted justification for these behaviors is electroconvection, an electro-osmotic instability resulting from concentration polarization at ion-selective interfaces. The convective

motions enhance the ion transport beyond simple diffusion through the formation of a mixing layer.

There have been a variety of theories proposed to explain the origins of this convective instability and the mixing it produces in electrochemical systems. The current theories predict that convection is a result of the formation of an extended space charge layer, many times the size of the equilibrium double layer [35,39,40]. For applied voltages beyond the thermal voltage (kT/e ≈ 25mV) ions begin to deplete at the surface of the ion-selective electrode and form concentration gradients near the electrode. As the voltage is increased further, a space charge layer forms from differences in cation and anion transport [41,42]. While both diffuse to the surface, the migration based on charge is opposite. For the example of a planar battery electrode at which charge storage occurs by cation deposition, this would create a space charge layer in which the cation concentration exceeds the anion concentration near the electrode.

At cell polarizations where the diffusional limit is approached, a region known as the extended space charge layer develops with a size given by equation 2

$$\epsilon \approx L\,(\hat{V}\hat{\delta})^{2/3} \tag{2}$$

From this equation it is apparent that the space charge layer thickness, ϵ, is related to the dimensionless voltage $\hat{V} \equiv V/V_T$, (where the thermal voltage $V_T \equiv \frac{kT}{e} = \frac{RT}{F}$) and dimensionless Debye screening length, $\hat{\delta} = \delta/L$ [43]. For typical experimental systems that will be explored in this thesis, this space charge layer can be as large as 10 μm. At a critical voltage (~$8V_T$), variations in charge distribution and/or roughness on the surface cause the space charge layer to impose a body force on the fluid, causing it to appear to slip relative to the surface. The slip velocity is therefore related to a

summation of terms linear and quadratic in $\hat{V}$ [37, 43]. Because of its similarity to the apparent slip (*electroosmotic slip*) produced by the action of an external electric field on the equilibrium space charge layer, this slip has been termed *electroosmotic slip of the second kind*. However, while this definition captures the essence of the hydrodynamics very close to the electrolyte/electrode boundary, it misses the complexity of the flow field produced by interaction of an external electric field and the non-equilibrium space-charge layer. Specifically, the fluid flow arising from this interaction tends to develop as a cascade of pairwise eddy structures as shown in figure 2a, which grow outward from the electrode/electrolyte interface. While such a flow is advantageous for enhancing ion transport in ion-flux limited processes such as desalination, it is problematic for the situation of electrodeposition. Because of the converging electroconvective rolls, ions are concentrated to points along the electrode surface. Additionally, experiments have shown that the rolls focus the transport to the tips of ramified structures as seen in figure 2b [19]. This tends to proliferate the unsteady growth, in turn compromising the electrodeposit, which creates problems in manufacturing or in the performance of a metal battery. Therefore, a more complete understanding of the underlying physics is needed. We believe that once these physics are in hand, rational approaches can be developed to either completely eliminate the underlying instabilities when they are unwanted, or to selectively enhance them in situations where they are beneficial.

1.3 Recent Developments

Overlimiting conductance has been studied for decades both in the context of desalination and electrodeposition. While the preliminary studies explored the cause of current exceeding the diffusion limit and the associated electric noise, more recent advances in theoretical work, experiments and direct numerical simulations have been able to more accurately probe the characteristics of the flow and to provide insights about how one might go about designing electrolytes and interfaces for its control.

Theoretical efforts using linear stability and perturbation analyses of the coupled Poisson Nernst-Planck and Stokes equations, have been reported that predict the eddy formation process and the transition to full-blown hydrodynamic instability [35,43, 45,46]. These analyses rely on the existence of an extended space charge layer and take

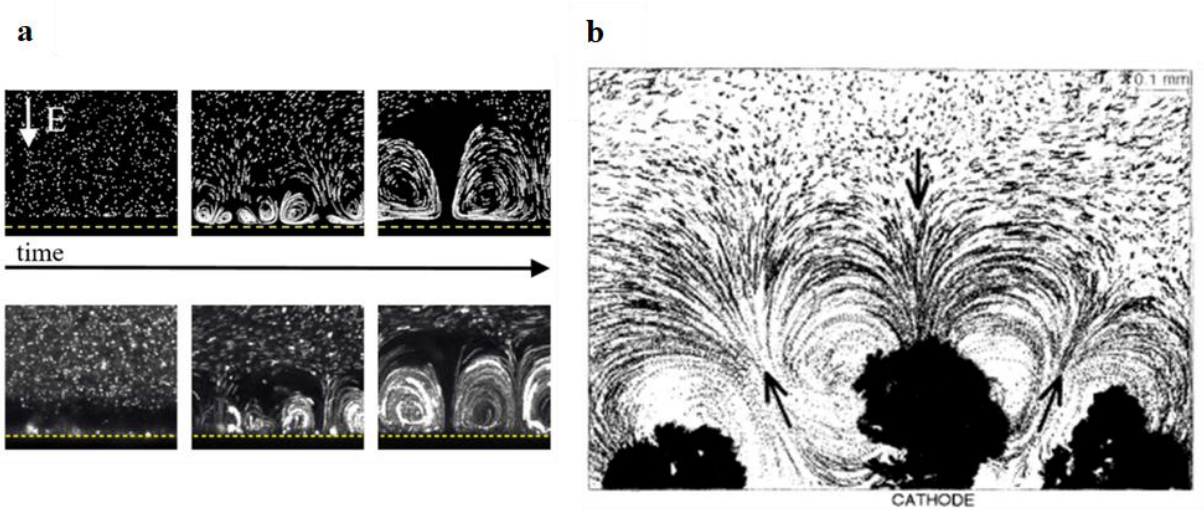

Figure 2: **a)** Snapshots from simulated (top) and experimental (bottom) tracer particles at an ion selective membrane (membrane is indicated by the yellow dashed lines). Simulations were performed at $40V_T$ and experiments were done at a current density of $1mA/cm^2$ in 10mM $CuSO_{4\,(aq)}$. Both techniques match qualitatively on the eddy structure of the convective flow [44]. **b)** Top view of convective motion visualized with tracer particles for 10mM $CuSO_{4\,(aq)}$ with a current density of $4mA/cm^2$ demonstrating the convection preferentially transporting to the tips of growing roughness elements [19].

this layer as the origin of the electroconvective flow. While the simplest linear stability analyses are able to predict the onset of electroconvection, analysis of the overlimiting regime requires a nonlinear treatment. The earliest solutions of the nonlinear problems utilized asymptotic approximations to solve the non-linear Nernst-Planck-Poisson (NPP) equations [35,47]. However, more recent reports raise serious doubt about the accuracy of the assumptions made to simplify the extended space charge layer [48]. These studies have found that with non-perfect ion selectivity at the interface, a different type of convection, equilibrium bulk electroconvection, dominates [49,50].

Direct numerical simulations (DNS) provides among the most powerful approach for understanding electroconvective flow and the hydrodynamic instabilities that produce overlimiting conductance and electric noise [39]. Mani and co-workers [48] for example developed a simple 2D simulation methodology that is able to solve the NPP equations rigorously without assuming a form for the underlying space charge layer. A highlight of the method has been the revelation of chaotic and multiscale flow fields at ion-selective interphases[48]. Although these flows originate from the right-hand-side of the linear momentum balance equations, from the coupling between the ion concentration field and the spatially varying electric potential, they exhibit features analogous to inertial turbulence. Importantly, DNS is also able to predict the two signature features of the electroconvective instability (overlimiting conductance and enhanced electric noise) observed in experiments [44].

These successes have motivated a number of DNS studies to probe the kinetic energy and forces associated with the convective motion as well as ion concentrations throughout an electrolyte with convection [51-53]. More recent efforts have shown how

the method can be extended to 3D domain to capture physics present under analogous conditions as those studied in experiments [51,54,55]. An interesting avenue for these simulations is to test techniques to control the convection within a system of interest. For example, work by Davidson et al. patterned a membrane surface with alternating permeable and impermeable portions [44]. The net result, after optimizing the pattern size was, that the transport can be enhanced beyond a fully permeable membrane, despite some portions of the surface being impermeable to ion motion. This technique is depicted in figure 3a. This technique has been tested experimentally and found to qualitatively match the simulation results [56,57].

Another notable example where DNS has been applied as a complementary tool to experiments comes from the recent work by Li et. al [58]. These authors coupled a spectral analytical method to DNS to investigate the effects of electrolyte viscoelasticity on electroconvective instability. An important finding from this work is that a viscoelastic electrolyte created by dissolving high molecular weight polymers in a simple liquid host stabilizes electrodeposition by introducing more unsteadiness in an electroconvective flow. In particular, Li et al showed that polymer stretching can disturb the vortex structure of the flow that causes ions to be focused to specific spots along an electrode surface.

Experimental techniques able to probe these phenomena and their fluid dynamic characteristics have developed significantly since the initial discovery. One early work was able visualize flow fields with tracer particles in an electrodeposition experiment [19]. This work established that both electroosmotic flows, due to electric fields, and buoyancy driven flows, due to gravity acting upon concentration gradients, are relevant

in many experimental setups. Additionally, it was found that these flows preferentially transport to the tips of rough deposits and play a major role in electrodeposition studies by altering the morphology of the deposit, shown in figure 2b. The first experimental visualization of the flow fields on a membrane surface was made by Rubinstein and coworkers in which polystyrene tracer particles were used to map the flow [59]. They were able to confirm the eddy-like structures of the flow and show that the size grew linearly with applied voltage. These results are shown in figure 4a. Studies have continued to develop and uncover new information about the nature of this instability, while still employing similar experimental cell setups and visualizing the motion of tracer particles. Recent works have confirmed the linear dependence of roll size with applied voltage [60,61]. This effect is shown in figures 4a,b in which the roll size grows with voltage. Multiple studies have also used dyes that respond to ion concentrations, which have enabled mapping of the concentration gradients with convective motions [19,60,62]. Through these studies the ion depletion region is confirmed to grow as the applied voltage grows. This technique has furthered the understanding of gravitational effects by visualizing the depleted regions impact on buoyancy driven flows [19,62]. The effects of gravity are apparent in figure 4c in which the direction of the electric field relative to gravity has a significant effect on the resulting convective flow.

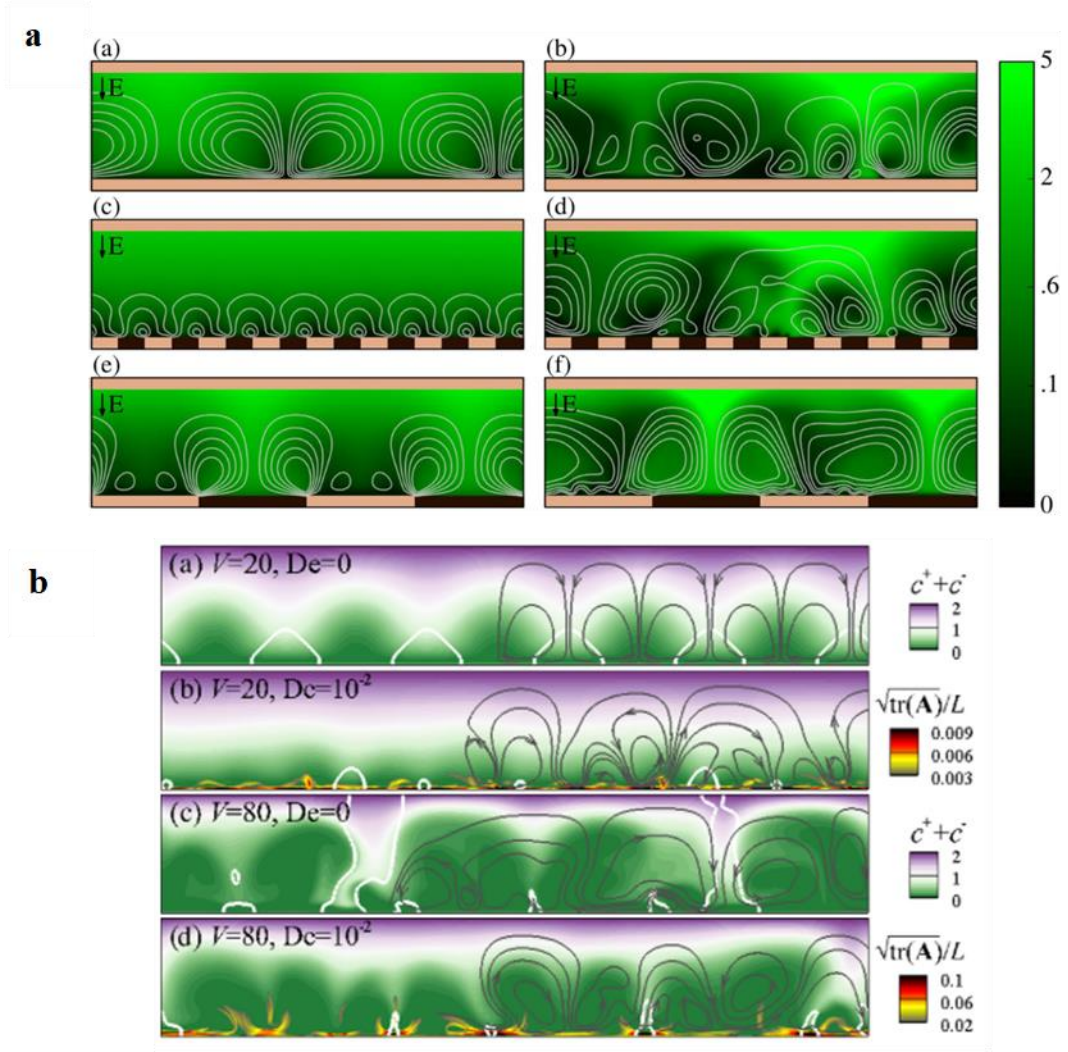

Figure 3: **a)** Snapshots of ion concentration fields for different membrane geometries where the dark portions are impermeable to ion transport. The left column is simulated at 20 V_T and the right column is at 60 V_T [44]. **b)** Plots of concentration with streamlines demonstrating the flow at different polarizations and Deborah numbers. The polymer extension ($\sqrt{tr(\boldsymbol{A})}/L$ is also highlighted for systems with a non-zero Deborah number [58].

Experiments have also been devoted to controlling these flows. The patterning effects that were derived from simulations have been studied experimentally. Both by patterning the transport length scales along a membrane and printing impermeable microgel patterns onto the membrane, the enhancement of transport that was predicted in simulations was verified [56,57]. A report by Wei et. al was able to demonstrate that viscoelastic electrolytes were able to delay the onset of electroconvective instabilities [63]. Through this they demonstrated these electrolytes were able to have stabilizing effect on the deposit morphology of Na and Li.

Even with the significant development in both aspects, comparisons between simulations and experiments have been limited thus far. There has been qualitative agreement between the flow images derived from simulations and experimental data, albeit under different conditions [44]. Additionally, the current and voltage data shows good agreement between these studies [39]. One of the main issues in connecting these two methods is a mismatch in the available length scale of the Debye layers. The Debye layer size, which is a function of electrolyte concentration, can be non-dimensionalized by the electrode gap in the cell. This dimensionless Debye layer size, $\hat{\delta}$, is typically on the order of 5×10^{-8} for an experiment in which the electrolyte concentration is 0.1M. If the concentration is dropped further to 0.1mM the theoretical $\hat{\delta}$ becomes 10^{-6}. In simulations, achieving small Debye layers is computationally difficult and has been limited to $\hat{\delta} > 10^{-4}$ [39]. Therefore, while qualitative comparisons can be made between these two methods there is a significant

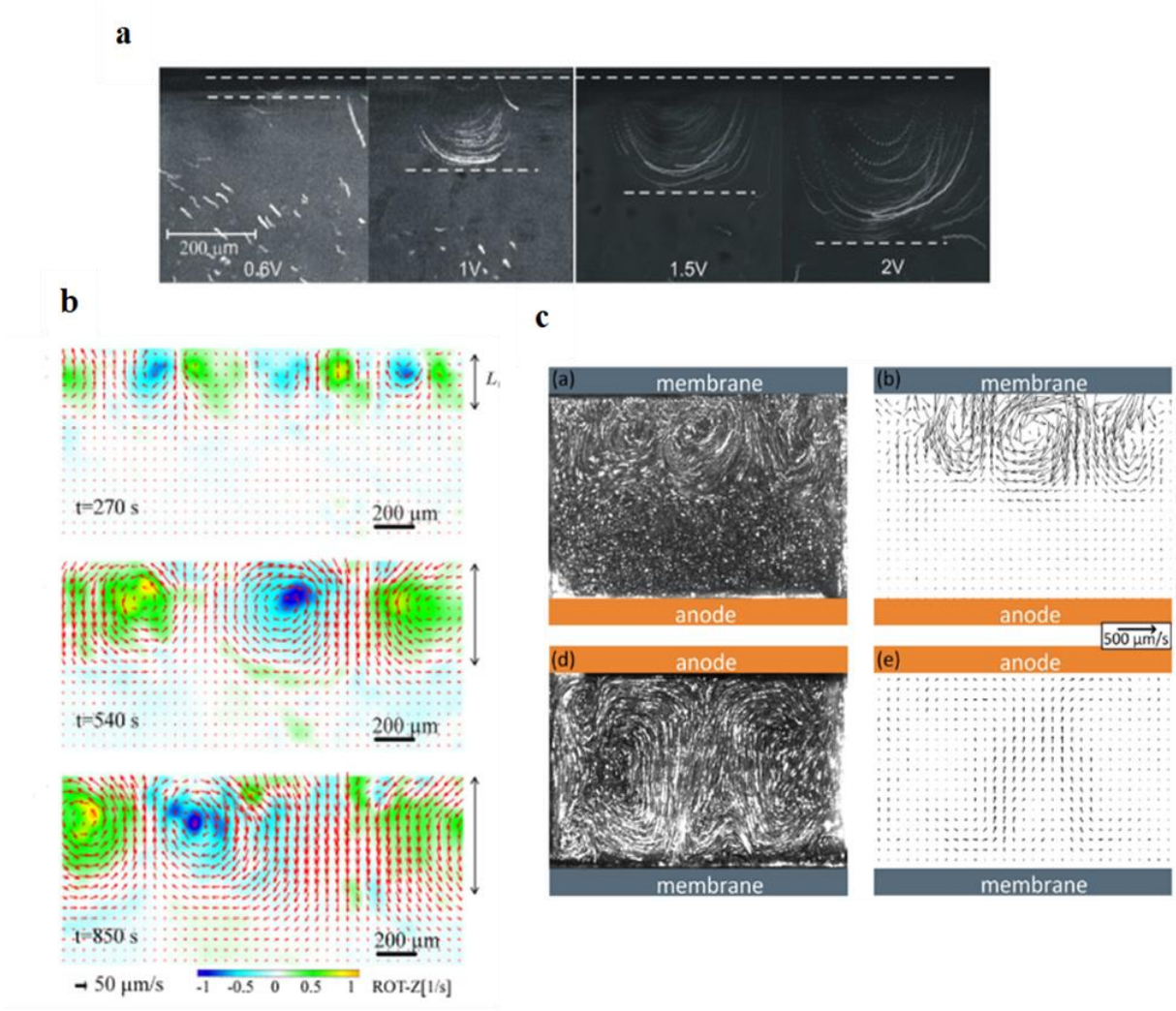

Figure 4: **a)** Time lapse images of tracer particle motion showing streamlines of convective flow for 0.01N $CuSO_{4\,(aq)}$. These images demonstrate the growth of convective rolls with voltage [59]. **b)** Vector maps of convective motion from particle tracking at different times in a 10mM $CuSO_{4\,(aq)}$ electrolyte. A constant current density of 1mA/cm^2 is applied and the voltage grows with time as the concentration polarization drives higher resistances [61]. **c)** Snapshots of particle motion (left column) and vector maps (right column) for 10mM $CuSO_{4\,(aq)}$ under a current density of 2.96mA/cm^2. The top figures are for the electric field (↑) and gravity (↓) in opposite directions and the bottom figures are for the both in the same direction (↓) [62].

gap in the ability to make quantitative comparisons without merging these length scales. Beyond that real experimental setups incorporate many non-idealities that are not accounted for in simulations. The visualization of flow is dependent on mapping tracer particle motion, but these tracers typically have some associated charge that can impact the flow and will respond to gravity if densities are not matched appropriately. Beyond this the true 3D convective rolls in experiments are deformed by gravitational influences. Further development in both areas is required to make quantitative comparisons and merge the understanding from both systems.

1.4 Outline

Many of the previous studies in the field of electroconvection have been devoted to desalination membranes and the role convective transport can play in that process. Beyond that the comparisons between simulation and experimental based studies have been limited. The goal of this thesis is to expand on those works with techniques that are fundamentally able to understand and control the flow in the context of metal electrodeposition. The control of convection both experimentally and in simulations has mostly been limited to the patterning of a membrane structure to enhance transport. This patterning method focuses convective transport to specific areas on the ion selective surface. This is highly advantageous for desalination where enhanced transport is the main goal and the localization of the ion transport will not hinder the performance of the process. However, in an electrodeposition process this focusing of the ion transport will be highly problematic as it will generate roughness elements. Patterning an electrode in a metal battery will inevitably increase the current density at the conductive portions, which is well known to enhance roughness as well. Studies of

a different control mechanism is necessary for the situation of electrodeposition.

The experimental visualization of electroconvection has been developing since the first study decades ago. Since then, studies have been able to confirm the growth of velocities and vortex sizes as functions of the voltage across a cell. Additionally, the time dependence of these flows has been analyzed. Dyes have even been used to visualize the ion concentration gradients that result from convective vortices. However, there is still a lack of connection from these experimental studies to direct numerical simulations of the systems. One main reason is the lack of overlap between the Debye length scales used. Experiments have been limited to small Debye length scales with constraints on electrolyte concentration and simulations have been limited to large Debye lengths with computational constraints. While a 1:1 comparison may not be currently feasible, understanding the effect of varying Debye lengths in experiments can allow for extrapolation to situations that can be modeled in simulations. Extracting data from these experiments that can be relevant to simulations, such as flow vectors and scaling laws, eases the comparisons that can be made.

In the following chapters I will lay out two studies in which I was able to fundamentally understand the effect of viscoelastic electrolytes on electroconvection and visualize the effects of Debye length and applied voltage on the structure of the convection. In Chapter 2, I will demonstrate that I was able to create viscoelastic liquid electrolytes in which momentum and ion transport were decoupled; the electrolytes had a high viscosity and liquid-like conductivities. These electrolytes consisted of high molecular weight polymers (~1 MDa) dissolved in carbonate-based lithium electrolytes. These electrolytes were tested to find the impact of polymer concentration on

overlimiting conductance. These tests were employed both in coin cells that utilized a metal electrode in which ions deposited and an ion selective Nafion-membrane to avoid a moving boundary that can impact the flow. The electrolytes were found to completely suppress an overlimiting conductance regime above the entanglement concentration of the polymers in both scenarios. This was verified in an experimental setup in which the convection was visualized. The speed of tracer particles in the system was found to reduce by an order of magnitude when the polymer additive was introduced. The motion was additionally found to be much less chaotic for the higher viscosity electrolyte. Through this technique of controlling the convection it is hypothesized that deposition roughness can be mitigated with the addition of high molecular weight polymers into electrolytes.

In Chapter 3 I expand upon the visualization studies to characterize the electroconvective flow structure of an aqueous copper electrolyte. This flow structure was studied over a range of voltages and Debye lengths to further the experimental understanding and create a better connection to numerical simulations. The convection was visualized at an ion selective Nafion membrane with neutral tracer particles and the particles were tracked using Particle Image Velocimetry. Vector fields were extracted to determine the effects of both voltage and electrolyte concentration on the resulting convection. The peak tangential velocity was found to scale approximately linearly with the applied potential. For higher applied potentials, the complexity of the flow structure was enhanced as multiple length scales of the flow were present. Changing the concentration has very minor effects on flow speed but reductions in concentration, accompanied by increases in Debye length, yielded more chaos in the flow. These larger

Debye lengths were found to incorporate more eddies sizes that propagate into the bulk. The ratio of small to large eddies is found to be a function of the dimensionless Debye length, $\hat{\delta}^{-1}$. This work was able to study the flow characteristics over a range of Debye lengths and applied potentials to enhance the comparisons that can be made between simulation and experimental based studies, and further the understanding of electroconvection that can happen in a variety of systems.

1.5 References

[1] Anuta, H., Ralon, P., Taylor, M., & La Camera, F. (2019). Renewable power generation costs in 2018. *International Renewable Energy Agency, Abu Dhabi*.

[2] Elliott, D. (2016). A balancing act for renewables. *Nature Energy, 1*(1), 1-3.

[3] Climate Change Division (2020). *Inventory of U.S. Greenhouse Gas Emissions and Sinks. 1990- 2018* (Report No. 430-R-20-002). U.S. Environmental Protection Agency.

[4] Armand, M., & Tarascon, J. M. (2008). Building better batteries. *Nature, 451*(7179), 652–657

[5] Tikekar, M. D., Choudhury, S., Tu, Z., & Archer, L. A. (2016). Design principles for electrolytes and interfaces for stable lithium-metal batteries. *Nature Energy*, *1*(9), 16114.

[6] Lin, D., Liu, Y., & Cui, Y. (2017). Reviving the lithium metal anode for high-energy batteries. *Nature Nanotechnology, 12*(3),194–206.

[7] Cheng, X. B., Zhang, R., Zhao, C. Z., & Zhang, Q. (2017). Toward Safe Lithium Metal Anode in Rechargeable Batteries: A Review. *Chemical Reviews, 117*(15), 10403–1047.

[8] Li, Y., & Dai, H. (2014). Recent advances in Zinc-air batteries. *Chemical Society Reviews, 43*(15), 5257-5275.

[9] Pei, P., Wang, K., & Ma, Z. (2014). Technologies for extending zinc–air battery's cyclelife: A review. *Applied Energy*, *128*, 315-324.

[10] Li, Q., & Bjerrum, N. J. (2002). Aluminum as anode for energy storage and conversion: a review. *Journal of power sources*, *110*(1), 1-10.

[11] Yang, H., Li, H., Li, J., Sun, Z., He, K., Cheng, H. M., & Li, F. (2019). The rechargeable aluminum battery: opportunities and challenges. *Angewandte Chemie International Edition*, *58*(35), 11978-11996.

[12] Lee, B., Paek, E., Mitlin, D., & Lee, S. W. (2019). Sodium metal anodes: Emerging solutions to dendrite growth. *Chemical reviews*, *119*(8), 5416-5460.

[13] Cheng, Xin-Bing, et al. "A review of solid electrolyte interphases on lithium metal anode." *Advanced Science* 3.3 (2016): 1500213.

[14] Sawada, Y., Dougherty, A., & Gollub, J. P. (1986). Dendritic and fractal patterns in electrolytic metal deposits. *Physical review letters*, *56*(12), 1260.

[15] Chazalviel, J. N. (1990). Electrochemical aspects of the generation of ramified metallic electrodeposits. *Physical review A*, *42*(12), 7355.

[16] Elezgaray, J., Léger, C., & Argoul, F. (1998). Linear stability analysis of unsteady galvanostatic electrodeposition in the two-dimensional diffusion-limited regime. *Journal of the Electrochemical Society*, *145*(6), 2016.

[17] Bard, A. J., Faulkner, L. R., Leddy, J., & Zoski, C. G. (1980). *Electrochemical methods: fundamentals and applications* (Vol. 2, p. 1). New York: Wiley.

[18] Sand, H. J. (1901). III. On the concentration at the electrodes in a solution, with special reference to the liberation of hydrogen by electrolysis of a mixture of copper sulphate and sulphuric acid. *The London, Edinburgh, and Dublin Philosophical Magazine and Journal of Science*, *1*(1), 45-79.

[19] Huth, J. M., Swinney, H. L., McCormick, W. D., Kuhn, A., & Argoul, F. (1995). Role of convection in thin-layer electrodeposition. *Physical Review E*, *51*(4), 3444–3458.

[20] Fleury, V., Chazalviel, J. N., & Rosso, M. (1993). Coupling of drift, diffusion, and electroconvection, in the vicinity of growing electrodeposits. *Physical Review E*, *48*(2), 1279–1295.

[21] Barkey, D. P., Watt, D., Liu, Z., & Raber, S. (1994). The role of induced convection in branched electrodeposit morphology selection. *Journal of the Electrochemical Society*, *141*(5), 1206.

[22] Bai, P., Li, J., Brushett, F. R., & Bazant, M. Z. (2016). Transition of lithium growth mechanisms in liquid electrolytes. *Energy Environ. Sci.*, *9*(10), 3221–3229.

[23] Costa, J. M., Sagués, F., & Vilarrasa, M. (1991). Growth rate of fractal copper electrodeposits: Potential and concentration effects. *Physical Review A*, *43*(12), 7057–7060.

[24] Bengoa, L. N., Pary, P., Seré, P. R., Conconi, M. S., & Egli, W. A. (2018). Dendritic Zinc Growth in Acid Electrolyte: Effect of the pH. *Journal of Materials Engineering and Performance*, *27*(3), 1103–1108.

[25] Nikonenko, V. V., Kovalenko, A. V., Urtenov, M. K., Pismenskaya, N. D., Han, J., Sistat, P., & Pourcelly, G. (2014). Desalination at overlimiting currents: State-of-the-art and perspectives. *Desalination*, *342*, 85–106.

[26] Kim, S. J., Ko, S. H., Kang, K. H., & Han, J. (2010). Direct seawater desalination by ion concentration polarization. *Nature Nanotechnology*, *5*(4), 297–301.

[27] Urtenov, M. K., Uzdenova, A. M., Kovalenko, A. V., Nikonenko, V. V., Pismenskaya, N. D., Vasil'eva, V. I., Sistat, P., & Pourcelly, G. (2013). Basic mathematical model of overlimiting transfer enhanced by electroconvection in flow-through electrodialysis membrane cells. *Journal of Membrane Science*, *447*, 190–202

[28] Seno, M., & Yamabe, T. (1963). Anomalous Conduction across Ion-exchange Membranes. *Bulletin of the Chemical Society of Japan*, *36*(7), 877–878.

[29] Fang, Y., Li, Q., & Green, M. E. (1982). Noise spectra of sodium and hydrogen ion transport at a cation membrane-solution interface. *Journal of Colloid And Interface Science*, *88*(1), 214–220.

[30] Yafuso, M., & Green, M. E. (1971). Noise spectra associated with hydrochloric acid transport through some cation-exchange membranes. *Journal of Physical Chemistry*, *75*(5), 654–662.

[31] Lifson, S., Gavish, B., & Reich, S. (1978). Flicker noise of ion-selective membranes and turbulent convection in the depleted layer. *Biophysics of Structure and Mechanism*, *4*(1), 53–65.

[32] Simons, R. (1979). Strong electric field effects on proton transfer between membrane-bound amines and water. *Nature*, *280*(5725), 824-826.

[33] Frilette, V. J. (1957). Electrogravitational transport at synthetic ion exchange membrane surfaces. *Journal of Physical Chemistry*, *61*(2), 168–174.

[34] Krol, J. J., Wessling, M., & Strathmann, H. (1999). Chronopotentiometry and overlimiting ion transport through monopolar ion exchange membranes. *Journal of membrane science*, *162*(1-2), 155-164.

[35] Rubinstein, I., & Zaltzman, B. (2000). Electro-osmotically induced convection at a permselective membrane. *Physical Review E - Statistical Physics, Plasmas, Fluids, and Related Interdisciplinary Topics*, *62*(2), 2238–2251.

[36] Rubinstein, I., & Maletzki, F. (1991). Electroconvection at an electrically inhomogeneous permselective membrane surface. *Journal of the Chemical Society,*

Faraday Transactions, *87*(13), 2079–2087.

[37] Rubinstein, I., & Zaltzman, B. (2001). Electro-osmotic slip of the second kind and instability in concentration polarization at electrodialysis membranes. *Mathematical Models and Methods in Applied Sciences*, *11*(2), 263–300.

[38] Rösler, H. W., Maletzki, F., & Staude, E. (1992). Ion transfer across electrodialysis membranes in the overlimiting current range: chronopotentiometric studies. *Journal of Membrane Science*, *72*(2), 171–179.

[39] Mani, A., & Wang, K. M. (2020). Electroconvection Near Electrochemical Interfaces: Experiments, Modeling, and Computation. *Annual Review of Fluid Mechanics*, *52*(1), 509–529.

[40] Zaltzman, B., & Rubinstein, I. (2007). Electro-osmotic slip and electroconvective instability. *Journal of Fluid Mechanics*, *579*, 173–226.

[41] Rubinstein, I., & Shtilman, L. (1979). Voltage against current curves of cation exchange membranes. *Journal of the Chemical Society, Faraday Transactions 2: Molecular and Chemical Physics*, *75*(6), 231–246.

[42] Rosso, M., Chazalviel, J. N., & Chassaing, E. (2006). Calculation of the space charge in electrodeposition from a binary electrolyte. *Journal of Electroanalytical Chemistry*, *587*(2), 323-328.

[43] Rubinstein, I., Zaltzman, B., & Lerman, I. (2005). Electroconvective instability in concentration polarization and nonequilibrium electro-osmotic slip. *Physical Review E - Statistical, Nonlinear, and Soft Matter Physics*, *72*(1).

[44] Davidson, S. M., Wessling, M., & Mani, A. (2016). On the Dynamical Regimes of Pattern-Accelerated Electroconvection. *Nature Publishing Group*, *March*, 1–10.

[45] Zaltzman, B., & Rubinstein, I. (2007). Electro-osmotic slip and electroconvective instability. *Journal of Fluid Mechanics*, *579*, 173–226.

[46] Schiffbauer, J., Demekhin, E. A., & Ganchenko, G. (2012). Electrokinetic instability in microchannels. *Physical Review E*, *85*(5), 055302.

[47] Yariv, E. (2009). Asymptotic current-voltage relations for currents exceeding the diffusion limit. *Physical Review E*, *80*(5), 051201.

[48] Druzgalski, C. L., Andersen, M. B., & Mani, A. (2013). Direct numerical simulation of electroconvective instability and hydrodynamic chaos near an ion-selective surface. *Physics of Fluids*, *25*(11), 110804.

[49] Rubinstein, I., & Zaltzman, B. (2015). Equilibrium electroconvective instability. *Physical Review Letters*, *114*(11), 114502.

[50] Pundik, T., Rubinstein, I., & Zaltzman, B. (2005). Bulk electroconvection in electrolyte. *Physical Review E*, *72*(6), 061502.

[51] Druzgalski, C., & Mani, A. (2016). Statistical analysis of electroconvection near an ion-selective membrane in the highly chaotic regime. *Physical Review Fluids*, *1*(7), 073601.

[52] Magnico, P. (2018). Spatial distribution of mechanical forces and ionic flux in electro-kinetic instability near a permselective membrane. *Physics of Fluids*, *30*(1), 014101.

[53] Davidson, S. M., Andersen, M. B., & Mani, A. (2013). Chaotic induced-charge electro-osmosis. *Physical Review Letters*, *112*(12), 1–5.

[54] Demekhin, E. A., Nikitin, N. V., & Shelistov, V. S. (2014). Three-dimensional coherent structures of electrokinetic instability. *Physical Review E*, *90*(1), 013031.

[55] Pham, S. V., Kwon, H., Kim, B., White, J. K., Lim, G., & Han, J. (2016). Helical vortex formation in three-dimensional electrochemical systems with ion-selective membranes. *Physical Review E*, *93*(3), 033114.

[56] Roghmans, F., Evdochenko, E., Stockmeier, F., Schneider, S., Smailji, A., Tiwari, R., Mikosch, A., Karatay, E., Kühne, A., Walther, A., Mani, A., & Wessling, M. (2019). 2D Patterned Ion-Exchange Membranes Induce Electroconvection. *Advanced Materials Interfaces*, *6*(1).

[57] De Valença, J., Jõgi, M., Wagterveld, R. M., Karatay, E., Wood, J. A., & Lammertink, R. G. H. (2018). Confined Electroconvective Vortices at Structured Ion Exchange Membranes. *Langmuir*, *34*(7), 2455–2463.

[58] Li, G., Archer, L. A., & Koch, D. L. (2019). Electroconvection in a Viscoelastic Electrolyte. *Physical Review Letters*, *122*(12), 124501.

[59] Rubinstein, S. M., Manukyan, G., Staicu, A., Rubinstein, I., Zaltzman, B., Lammertink, R. G. H., Mugele, F., & Wessling, M. (2008). Direct observation of a nonequilibrium electro-osmotic instability. *Physical Review Letters*, *101*(23), 236101.

[60] Kwak, R., Guan, G., Peng, W. K., & Han, J. (2013). Microscale electrodialysis: Concentration profiling and vortex visualization. *Desalination*, *308*, 138–146.

[61] De Valença, J. C., Wagterveld, R. M., Lammertink, R. G. H., & Tsai, P. A. (2015). Dynamics of microvortices induced by ion concentration polarization. *Physical Review E - Statistical, Nonlinear, and Soft Matter Physics*, *92*(3), 031003.

[62] De Valença, J. C., Kurniawan, A., Wagterveld, R. M., Wood, J. A., & Lammertink, R. G. H. (2017). Influence of Rayleigh-Bénard convection on electrokinetic instability in overlimiting current conditions. *Physical Review Fluids*,

2(3), 033701.

[63] Wei, S., Cheng, Z., Nath, P., Tikekar, M. D., Li, G., & Archer, L. A. (2018). Stabilizing electrochemical interfaces in viscoelastic liquid electrolytes. *Science Advances*, *4*(3), 1–9.

Chapter 2: Electrokinetics in Viscoelastic Liquid Electrolytes Above the Diffusion Limit

2.1 Introduction

Electrodeposition of metals is a fundamentally unstable process at high ionic currents. Its stability has been studied for over one hundred years in the context of electroplating but has reemerged in recent years as a crucial impediment to next generation batteries that utilize high capacity, energetic metals such as zinc, aluminum, and lithium as anodes [1]. At high rates, recharge of any of these metals produce concentration polarization in liquid electrolytes, which is known to drive a hydrodynamic instability termed electroconvection. Early work has shown that the instability causes nonuniform transport of metal cations to the interface, leading to the rough electrodeposits loosely termed dendrites during battery charging [2-4]. Concentration polarization in an electrochemical cell is a consequence of selective reduction of cations at the anode surface, which depletes cations from the electrolyte. Local charge balance requires diffusion of cations from elsewhere in the cell to compensate the depleted charge. Charging a battery at current densities that exceed the diffusion limit therefore produces a region near the electrode termed the extended space charge regime, in which electroneutrality cannot be maintained at all times [4,5], and which extends much further into the electrolyte bulk than the equilibrium space charged formed at the interface between any charged substrate in an electrolyte.

A similar process has been studied at interfaces formed between cation-selective/exchange membranes that restrict the passage of anions [6]. In this latter case,

formation of the space charge is decoupled from the boundary condition at the interface and the consequences of the space charge region on the local electric field, fluid trajectories, and ion migration profiles can be analyzed in greater detail. On the basis of theory [7,8], numerical simulations [9,10], and a limited set of experiments [11,12] current thinking is that the large and non-uniform electric field required to maintain an imposed current/ion flux through the space charge region couples with the charged fluid to create a body force that drives fluid motion in the cell. This force is analogous to that which drives electroosmotic flow in any electrolyte when an external electric field interacts with the equilibrium space charge formed at an electrified interface immersed in a liquid electrolyte, and the convective rolls it produces have been termed electroosmotic flow of the second kind [7,13]. Because electroconvective rolls preferentially transport ions to the tips of dendrites and increases the roughness of electrodeposits [2,8,14], they also exacerbate morphological instabilities known to produce rough dendritic electrodeposition of metals.

Polarization of the ion distribution in a liquid electrolyte produces density gradients in the electrolytes, which under the action of gravity can complicate experimental analysis of electroconvection. The orientation of gravity relative to the electric field provides a relatively straightforward empirical constraint for limiting/increasing the influence of gravity [15]. In the *gravitationally stable configuration*, the imposed electric field in the cell is opposite to gravity, meaning that density gradients limit the extension of electroconvective flow patterns. The opposite is true for the *gravitationally unstable configuration*, in which gravity can facilitate the destabilization of electroconvection. The importance of gravitational forces relative to the viscous forces that must be

overcome to produce fluid motion as a result of ion electromigration can be quantified in terms of the nondimensional Rayleigh number, $Ra = \beta \Delta c g L^3/\nu D$. Here, β is the *solute expansion coefficient*, L is the gap between the electrodes of interest, g is the acceleration due to gravity, Δc is the change in concentration, and ν and D are the kinematic viscosity and diffusion coefficient, respectively. For Rayleigh numbers greater than a critical value of approximately 1,000, gravitational effects cannot be ignored.

Here, we investigate the effects of high molecular weight polymer additives on the stability of this second kind electroosmotic flow. Our study is motivated by recent experiments by Wei et al.[16], which show that at concentrations as low as 4% by weight, high molecular weight polymer additives in liquid electrolytes impart viscoelasticity to the electrolytes, which suppress hydrodynamic instability during recharge of a metal electrode in liquid electrolytes. Here we wish to remove complications arising from changes in the boundary condition at an advancing metal electrodeposit front, to facilitate more detailed understanding of the role electrolyte viscoelasticity plays in regulating electroconvection at interfaces formed between an ion selective membrane and liquid electrolyte. As in the study by Wei et al. [16], we will show that at sufficiently high polymer additive molecular weights where polymer chains entangle in solution, the polymer additive has a much larger effect on momentum transport in the electrolyte, in comparison to its impact on ion transport. The large increase in viscosity and elasticity imparted by the polymer are further shown to extend the limiting current plateau in electrokinetics experiments and dramatically reduce the intensity of electroconvective flows. Both effects are, in turn, shown to be insensitive

to electrolyte or polymer chemistry. Our results, therefore, imply that provided the selected polymer additive is electrochemically stable at the measurement conditions, any long-chain polymer with the ability to entangle at low concentrations to maintain high ionic conductivities while imparting viscoelasticity to the electrolyte should suffice.

2.2 Results and Discussion

Aprotic liquid electrolytes composed of a 1:1 volume ratio mixture of ethylene carbonate (EC) and propylene carbonate (PC) containing 0.1M and 1M Lithium bis(trifluoromethane)sulfonimide salt were used in the majority of the studies reported in this paper. An electrochemically inert polymer poly(methyl methacrylate) (PMMA) (M_w = 0.996 x 10^6 g/mol), was dissolved in these electrolytes to create viscous liquids with polymer concentrations up to 10 percent by weight. Electrokinetics in the resultant viscoelastic liquid electrolytes were studied in two electrochemical cell geometries: (i) symmetric Li||Li cells (figure 9a) in which PTFE (Teflon) washers with thickness of 0.8mm were used as spacers between the electrodes; and (ii) asymmetric Li||Cu cells (figure 10a) in which a Nafion NRE 212 cation-selective membrane (Sigma Aldrich) was placed on top of the copper-facing side of the PTFE washer. In either geometry, current voltage profiles were recorded from time-dependent voltage ramp measurements using a Maccor Series 4000 Battery Tester. Rheological properties of all electrolytes used in the study were investigated in a small-amplitude oscillating shear using an Anton Paar MCR Rheometer outfitted with cone and plate fixtures with a fixed cone angle of approximately 1°. The D.C. ionic conductivity of the electrolytes was measured as a function of polymer concentration using a Novocontrol N40 Broadband

Dielectric Spectrometer at temperatures in the range 10°C -95°C. Electrokinetics studies were complemented with flow visualization of polystyrene tracer particles (average diameter = 10μm) dispersed in aqueous 10mM $CuCl_2$ electrolytes containing 0, 0.5 and 1wt% of an ultrahigh molecular weight PEO ($M_w = 8*10^6$ g/mol). Measurements were performed in an optical cell (figure 12a) composed of 0.55mm thick copper electrodes at a fixed gap separation of 1.25cm. Voltage control for these experiments was achieved using a Neware CT-3008 Battery Tester.

We investigated electrokinetics in the aprotic liquid electrolytes by recording the current-voltage (*i*-V) profiles as a function of polymer concentration. In these tests a longer plateau in the diffusion limited regime signals a suppression of convection. On this basis we show later that it is possible to extend that stable voltage window to arbitrarily high values (in many cases to values outside the electrochemical stability window of the electrolyte solvent) by simply increasing the concentration of polymer. Our goal is to perform experiments where transport effects dominate electrochemical changes at the electrodes, which requires conditions where the diffusion boundary layer thickness spans much of the inter-electrode space. To achieve such conditions, we imposed voltages in the range of 0V to 5V (the upper limit for electrolyte breakdown) in a step-ramp protocol (each step lasted for 5 mins shown in figure 9) and recorded the average current at the end of each step.

The cell configuration depicted in figure 9a was used to represent a system in which morphological changes associated with metal deposition influences the boundary conditions experienced by an electrolyte in the electrokinetics studies. This couples both the hydrodynamic and morphological instabilities associated with high current

deposition of metals. These experiments were complemented with others in a second cell configuration (see figure 10a) in which a lithium metal counter electrode was used as a supply of lithium ions and a Nafion^{TM} membrane used as an ion selective membrane, to study the depletion of the ions without the possibility of morphological instabilities. To fully understand the extent to which a viscoelastic electrolyte can stabilize electroconvection, all cells were mounted in the gravitationally unstable configuration.

At the lower salt concentration of 0.1M LiTFSI the Rayleigh number is approximately unity at 10wt% PMMA, 200 for an electrolyte with 5wt% PMMA, and $2.1*10^5$ for the control. The resulting *i*-V curves obtained from the symmetric cell experiments are reported in Figure 5a. It is apparent that for electrolytes with polymer concentrations under 3.5wt% the current begins to diverge with polarization under 1V. Furthermore, at higher polymer concentrations the diffusion limited plateau is seen to be extended. Figure 5b investigates the effect of electrolyte viscosity on the width ΔV of the diffusion-limited transport regime. The results show that a rough scaling relationship $\Delta V \sim \eta^{0.5}$ can be defined for the first four points, after which the voltage window is determined by the end point of the test. However, the expectation is that the effect of viscosity saturates above the 5%. This two-stage relationship between ΔV and η is also evident in the earlier study by Wei [16], but is in closer accord with expectations from our recent theoretical study of electroconvection in entangled polymers, where ΔV was shown to exhibit a progressively weaker dependence on η (from $\Delta V \sim \eta^{0.5}$ to $V \sim \eta^0$) as the localized (on length scales of order the solution correlation length) drag chains exert on an electrolyte solvent are made progressively smaller[17].

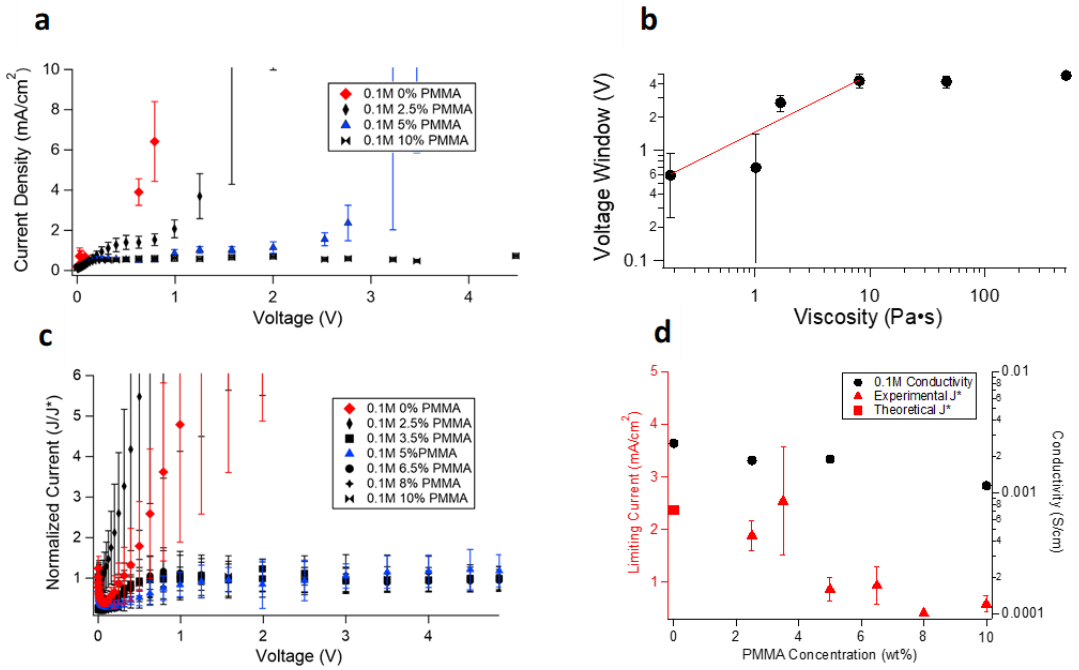

Figure 5: **a)** Current voltage diagrams obtained using symmetric lithium Li||Li cells and aprotic liquid electrolytes with varying PMMA concentration. Even at relatively low PMMA concentrations, large enhancements of the width of the diffusion-limited ion transport plateau are observed. **b)** The voltage window or length of the plateau region from the current voltage diagram is plotted as a function of the electrolyte viscosity. The red line is a best-fit to the data and supports the relationship $\Delta V \sim \eta^{0.5}$. **c)** Current voltage diagrams obtained using Li||Cu cells with an ion-selective membrane used to isolate hydrodynamic effects from morphological changes at the electrode. **d)** The conductivity and limiting current measured as functions of polymer concentration. It is evident that while the bulk conductivity of the electrolyte remains relatively constant, the limiting current is largely reduced at polymer concentrations above the entanglement threshold (~5%).

Figure 5c shows the results for the analogous experiment where an ion selective membrane is employed. Here we normalized the recorded currents by the empirical or calculated diffusion limiting current to facilitate the comparisons. In this presentation, any value of the normalized current density that exceeds 1 would be defined as an overlimiting current. For polymer concentrations below 3.5wt%, we find that

overlimiting conductance proceeds essentially unchecked by electrolyte viscoelasticity, however, for PMMA concentrations of 3.5wt% and higher, the diffusion-limited plateau is extended indefinitely (at least up to 5V, where the electrochemical stability of the electrolyte solvent limits the experiment). Our findings imply that overlimiting conductance is essentially eliminated at an ion selective membrane in electrolytes above the concentration which will be shown to be near the entanglement threshold. Results reported in figure 10b, show that this effect is sensitive to the electrolyte salt concentration and the PMMA concentration at which overlimiting conductance is arrested shifts to higher values at higher salt concentrations. This finding is consistent with our recent findings from direct numerical simulations of viscoelastic liquid electrolytes that the magnitude of the electroconvective slip velocity rises as the Debye screening length in the electrolyte becomes smaller [18]. We hypothesize that polymer elasticity is effective in suppressing hydrodynamic instability, which is considered responsible for overlimiting conductance.

As a first test of this hypothesis, we compare our findings with a recent theoretical study where we employed linear stability analysis of a two-fluid polymer model to determine the effect of entangled polymers on the hydrodynamic, as well as coupled morphological and hydrodynamics, instability [17]. In qualitative agreement with the experimental observations, the theory shows that entangled polymers suppress hydrodynamic instability by selectively imposing stronger drag on the electrolyte solvent than on ions in solution. Support for this framework in turn comes from Figure 5d where we report limiting currents and conductivities for the range of polymer concentrations studied. For the control and weakly entangled electrolytes, where

overlimiting conductance is strong and a clear diffusion-limited current plateau is not observed, the limiting current values correspond to the theoretical limiting current deduced from the measured electrolyte conductivity, which are generally higher than the measured values in simple Newtonian liquid electrolytes [19,20]. The results show that both the limiting current and conductivity are weaker functions of polymer concentration than the electrolyte viscosity, consistent with the two-fluid framework upon which the linear stability analysis builds.

The physical properties of the designed electrolytes were evaluated using a suite of analytical methods. Figure 6a reports the dynamic storage (G') and loss (G'') moduli of the electrolytes at 25^{o}C as a function of polymer concentration. Analysis of the results for the 0.1M LiTFSI electrolytes reveal that above a concentration of approximately 5 weight percent of the PMMA the loss modulus surpasses the storage modulus at high frequency. This implies that our electrolytes transition from nominally viscous liquids ($G'' > G'$ over the full frequency range explored) to viscoelastic fluids, wherein $G' > G''$ only at higher ω. The transition from liquid to viscoelastic fluid behavior can be used to infer microscopic information about the configuration of the polymer chains in solution; it may be used for example to deduce that above a polymer concentration of 5wt% the PMMA chains form physical entanglements in the electrolyte solution [21].

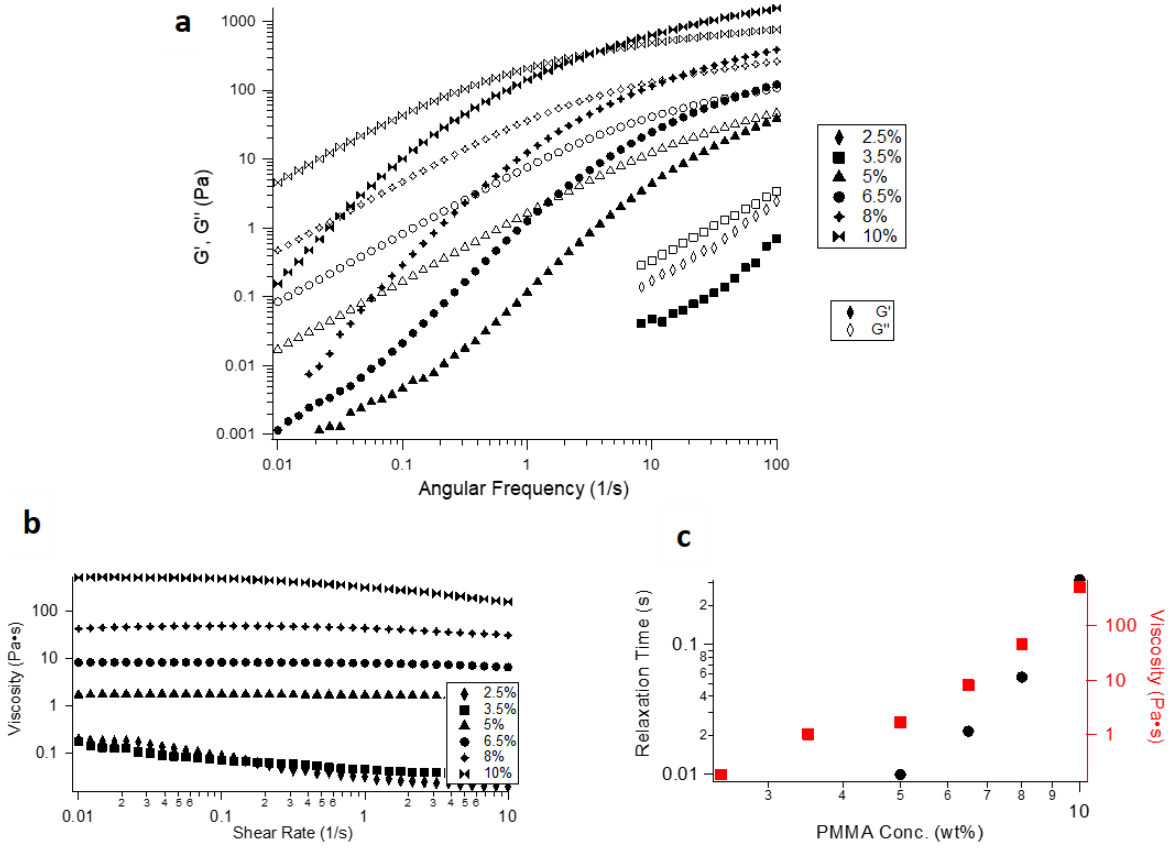

Figure 6: **a)** Frequency-dependent storage (*G'*) and loss (*G''*) moduli deduced from small-amplitude oscillatory shear rheology measurements using 0.1M LiTFSI in EC/PC aprotic liquid electrolyte with varying PMMA concentration. The *G'* for the 2.5% electrolyte are not shown because the measured values are below the detection limit of the rheometer used in the study. **b)** Shear rate sweep rheology of the same electrolytes demonstrating that as polymer concentration increases there is a transition from Newtonian to non-Newtonian shear thinning rheological behavior. **c)** The dependence of electrolyte relaxation time and viscosity as a function of polymer concentration.

The apparent viscosity of the electrolytes was determined using a shear rate sweep rheological method in which electrolyte solutions are subjected to a constant shear rate at 25°C and the long-time/steady-state viscosity at each rate is measured. Results from these experiments are reported in Figure 6b and show that for polymer concentrations above 5wt% the electrolytes transition from a Newtonian fluid state (wherein viscosity

is independent of shear rate) to a non-Newtonian, shear-thinning state in which the viscosity decreases with increasing rate. The time scale for

polymer relaxation can be extracted from the inverse of the frequency at which the loss and storage moduli crossover in the previous oscillatory shear measurements [22,23]. Figure 6c plots this time scale and the Newtonian viscosity of the electrolytes as a function of polymer concentration. Above the critical concentration of 5wt%, the characteristic polymer relaxation time and viscosity follow the relationships, $\lambda \sim c^{4.91}$, and $\eta \sim c^{8.22}$, respectively. These power-law scalings are slightly higher than those reported previously [24,25] , but are consistent with our microscopic picture that above a concentration of approximately 5wt%, the PMMA chains in the electrolyte form an entanglement network that produces the large enhancements in fluid viscosity.

The conductivity of the electrolytes are reported in Figure 7a. The solid lines through the data are best fit curves obtained using the VFT equation [26]; the apparent activation energies extracted from the fits are reported in figure 11a. Comparing the effects of polymer concentration on conductivity and viscosity (Figure 7b), it is clear that the conductivity remains relatively constant while the viscosity increases significantly at high polymer concentrations. It is also significant that the activation energies deduced from the VFT fits of the temperature-dependent conductivity also remain relatively independent of polymer concentration. We interpret these observations to mean that the polymer additives have little impact on ion motion in the system.

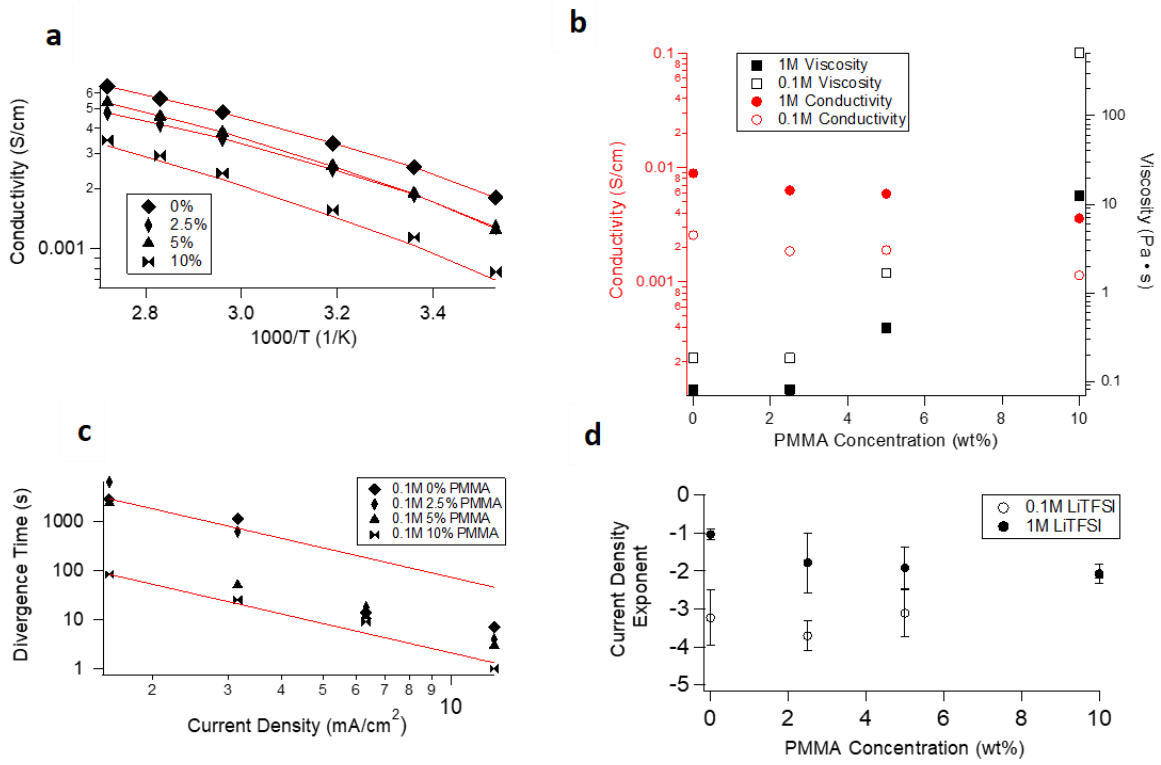

Figure 7: **a)** D.C. conductivity of electrolytes as a function of temperature. The red lines are VFT fits for the conductivity data. **b)** Conductivity and viscosity represented as a function of polymer concentration. It is evident that the conductivity decrease is relatively small compared with the large increase in viscosity as polymer concentration increases. **c)** Voltage divergence time (for constant current tests) shown as a function of current density. The red lines are guides for the theoretical relationship of $t_{div} \sim J^{-2}$. **d)** Results of fitting the current density exponent for the different concentration of polymers. Theoretically the exponent should be -2 and this is best shown for high polymer concentration and the 1M concentration of salt.

The most straightforward approach for characterizing ion polarization at an interface is to measure the voltage required to maintain a specified (controlled) current density as a function of time. For current densities above the diffusion limit, ion polarization causes the voltage to diverge on a certain current-density dependent timescale termed the Sand's time [27,28]:

$$t_{sand} = \pi D \frac{(z_c c_0 F)^2}{4(J t_a)^2}$$

Here D is the diffusion coefficient, z_c is the cation charge number, c_0 is the bulk concentration, F is faraday's constant, J is the current density, and t_a is the anion transference number. The coin cell configuration depicted in supporting figure 9a was used to characterize voltage versus time profiles. After a certain period of time, the voltage begins to diverge, an example plot is shown in figure 11b. By performing these chronoamperometric measurements for electrolytes over a range of polymer concentrations and current densities, the voltage divergence time t_{div} was determined for a range of electrolyte compositions and at various current densities (Figure 7c)**.** The lines through the figure are provided as guides to the eye to aid visual comparison of the measured versus current density with the theoretical scaling, $t_{div} \approx t_{sand} \sim J^{-2}$, expected from the definition of the Sand's time at which polarization of the electrolyte leads to a deficit of anions at the electrode surface. For both salt concentrations studied, the measured t_{div} is observed to decrease in proportion to the electrolyte viscosity but decreases much faster than expected from the electrolyte conductivity, implying that the Nernst-Einstein relationship breaks down in these electrolytes. More quantitative comparisons of the scaling exponents are provided in Figure 7d where it is observed that agreement between the measured and predicted exponents is best in electrolytes with 1M salt concentration and at higher polymer concentrations. This establishes that even with the addition of polymers, ions deplete at the surface in a predictable manner. As a more concrete assessment of our hypothesis that polymer elasticity suppresses hydrodynamic instability of liquid electrolytes at ion-selective interfaces, we turn to direct visualization studies of electrolyte dynamics. For this purpose, we constructed an optical cell (see figure 12a) and employed tracer particle velocimetry to directly

analyze fluid motions near ion-selective interfaces. Because these experiments require long data collection times and large throughput of metal, they cannot be performed safely using Li electrodes. Here we instead utilize copper as the working electrode and an aqueous copper electrolyte. The rheological properties of these electrolytes are similar to the lithium electrolytes studied (figure 12b,c) with an entanglement transition between 0.5wt% and 1wt%. Experiments were performed at voltages varying from 0.25V to 5V between copper electrodes with Nafion^{TM} employed as an ion-selective, separating membrane. By visualizing particle trajectories at the electrolyte/ Nafion^{TM} interface over a range of voltages, it was possible to characterize how the hydrodynamic instability develops and what role electrolyte viscoelasticity plays in that development. Videos from 0-1wt% polymer have been taken, which clearly show that strong convective motions emerge in the quiescent liquid electrolyte. The main features of this motion are illustrated in Figure 8a using maps of the particle velocity profiles for the control electrolyte at 5V. The results clearly show that strong convective rolls develop quickly at the interfaces and that there are two distinct length scales in which the convection manifests. Large macroscopic rolls, comparable in size to the inter-electrode spacing, coexist with smaller, turbulent flow structures localized near the interface and in which the fluid velocity is higher, fluid trajectories more variable in space and time, and fluid flow lines exhibit higher curvatures. The larger roles are consistent with observations from previous direct numerical simulations by Mani's group [9,10]. These effects can be compared to those seen in Figure 8b for the same polarization but with the addition of 1wt% PEO. For the same elapsed time (3 minutes) there is significantly more motion and turbulence for the control case. Visual inspection of the videos clearly

show that the electrolyte viscoelasticity has a more obvious effect on the large rolls than on the smaller, more turbulent features. To quantify this effect, we report in Figure 8c the average velocity deduced from the videos using Trackmate software [29] at various potentials and polymer concentrations. The results demonstrate that as polymer concentration increases, the velocity of the resulting convective rolls decrease by more than one order of magnitude. The results show further that as the polymer concentration increases a higher voltage is required to initiate electroconvection, which explains the extension of the diffusion-limited ion transport regime observed in the previously shown *i*-V curve.

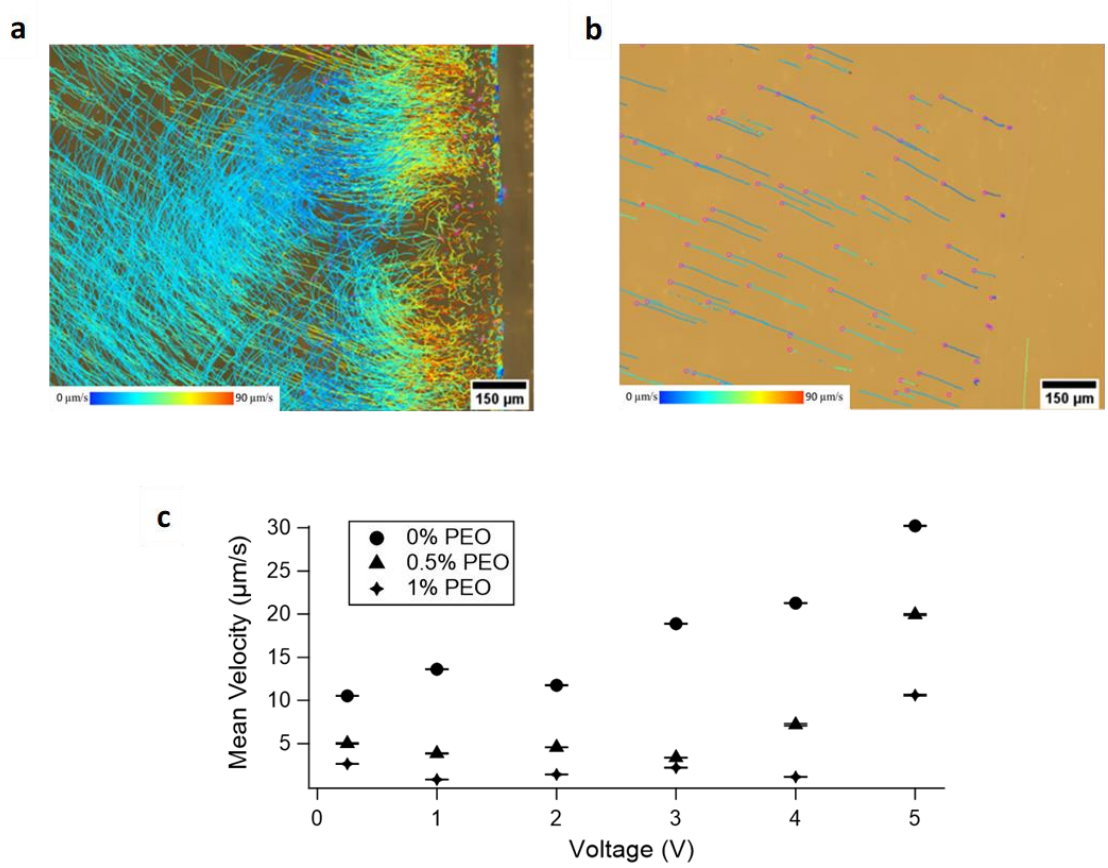

Figure 8: **a,b)** Example velocity maps for control and 1wt% PEO respectively under 4V polarization. Both maps encompass 3 minutes of particle tracking, which exhibits the significantly higher motion and turbulence in the control relative to the 1wt% polymer. **c)** The average particle velocity as a function of voltage for 0, 0.5 and 1wt% PEO in the system. For each voltage the control case has higher velocities and it is even more evident when turbulent convection sets in at 3V.

2.3 Conclusions

Next generation batteries that contain metal anodes require electrolytes that have high conductivities, are chemically and thermally stable at high voltages, and which provide fundamental mechanisms for stabilizing intrinsically unstable electrodeposition at high current densities. We report that addition of high molecular weight polymers to either

aprotic liquid or aqueous electrolytes provides a facile method for imparting viscoelasticity to these electrolytes while minimally impacting conductivity. At moderate polymer concentrations, analysis of the *i*-V curve for viscoelastic electrolytes bounded either by metal or ion-selective polymer interfaces show that the diffusion-limited transport regime can be extended indefinitely and that overlimiting conductance can be completely suppressed in electrochemical systems where coupling between morphological and hydrodynamic instability is eliminated. Finally, by directly visualizing the motions of micron-size, neutral tracer particles in the electrolyte bulk and near ion-selective interfaces, we report that hydrodynamic instability leads to qualitatively different electroconvective flows on small and large length scales. We also find that the average fluid velocity in an entangled polymer electrolyte is lowered by more than one order of magnitude, with the largest suppression occurring at the highest cell voltages where hydrodynamic instability is strongest.

2.4 References

[1] Bancroft, Wilder D. The Chemistry of Electroplating. *J. Physical Chemistry* **1905,** *9*, 277-296.

[2] Barkey, D. P., et al. The role of induced convection in branched electrodeposit morphology selection. *J. Electrochemical Society* **1994,** *141*, 1206-1212.

[3] Rosso, M., et al. Experimental evidence for gravity induced motion in the vicinity of ramified electrodeposits. *Electrochimica Acta* **1994,** *39*, 507-515.

[4] Huth, John M., et al. Role of convection in thin-layer electrodeposition. *Physical Review E* **1995,** *51*, 3444-3458.

[5] Block, M. & Kitchener, J. A. Polarization phenomena in commercial ion-exchange membranes. *J. Electrochemical Society* **1966,** *113*, 947–953.

[6] Chazalviel, J. N. Electrochemical aspects of the generation of ramified metallic electrodeposits. *Physical Review A* **1990,** *42*, 7355–7367.

[7] Zaltzman, B. & Rubinstein, I. Electro-osmotic slip and electroconvective instability. *J. Fluid Mechanics* **2007,** *579***,** 173-226.

[8] Fleury, V., Kaufman, J., & Hibbert, B. Evolution of the space-charge layer during electrochemical deposition with convection. *Phys. Rev. E **1993,** 48*, 3831-3840.

[9] Davidson, S. M., Wessling, M., & Mani, A. On the Dynamical Regimes of Pattern-Accelerated Electroconvection. *Scientific Reports **2016**, 6*, 22505.

[10] Demekhin, E. A., Nikitin, N. V. & Shelistov, V. S. Direct numerical simulation of electrokinetic instability and transition to chaotic motion. *Physics of Fluids* **2013,** *25*, 122001.

[11] de Valença, J. C., Wagterveld, R. M., Lammertink, R. G. H. & Tsai, P. A. Dynamics of microvortices induced by ion concentration polarization. *Phys. Rev. E* **2015,** *92*, 031003.

[12] Nam, S., et al. Experimental verification of overlimiting current by surface conduction and electro-osmotic flow in microchannels. *Physical Review Letters* **2015**, *114*, 114501.

[13] Rubinstein, I. & Zaltzman, B. Electro-osmotically induced convection at a permselective membrane. *Physical Review E* **2000,** *62*, 2238-2251.

[14] Nishida, T., Nishikawa, K., Rosso, M. & Fukunaka, Y. Optical observation of Li dendrite growth in ionic liquid. *Electrochimica Acta* **2013**, *100*, 333-341.

[15] Karatay, E., et al. Coupling between buoyancy forces and electroconvective instability near ion-selective surfaces. *Physical Review Letters* **2016,** *116*, 194501.

[16] Wei, S. et al. "Stabilizing electrochemical interfaces in viscoelastic liquid electrolytes. *Science Advances* **2018**, *4*, 6243.

[17] Tikekar, M. D., et al. Electroconvection and Morphological Instabilities in Potentiostatic Electrodeposition across Liquid Electrolytes with Polymer Additives. *J. Electrochemical Society* **2018**, *165*, A3697-A3713.

[18] Li, G.; et al. Electroconvection in a viscoelastic electrolyte. *Phys. Rev. Lett.* **2019**, *122*, No. 124501.

[19] Maletzki, F., Rösler, H.-W., E. Staude, E. Ion transfer across electrodialysis membranes in the overlimiting current range: Stationary voltage current

characteristics and current noise power spectra under different conditions of free convection. *J. Membr. Sci*. **1992**, *71*, 105–116.

[20] Rubinshtein, I., Zaltzman, B., Pretz, J., Linder, C. Experimental verification of the electroosmotic mechanism of overlimiting conductance through a cation exchange electrodialysis membrane. *Russ. J. Electrochem.* **2002**, *38*, 853–863.

[21] Tung, C-Y. & Dynes, P. J. Relationship between viscoelastic properties and gelation in thermosetting systems. *Journal of Applied Polymer Science* **1982**, *27*, 569-574.

[22] Volpert, E., Selb, J. & Candau, F. Associating behaviour of polyacrylamides hydrophobically modified with dihexylacrylamide. *Polymer* **1998,** *39*, 1025-1033.

[23] Castelletto, V., et al. Rheological and structural characterization of hydrophobically modified polyacrylamide solutions in the semidilute regime. *Macromolecules* **2004**, *37* 1492-1501.

[24] Berry, G. & Fox, T. G. The viscosity of polymers and their concentrated solutions. *Adv. Polymer Sci.* **1968,** *5*, 261-357.

[25] Cho, J., et al. Viscoelastic properties of chitosan solutions: Effect of concentration and ionic strength. *Journal of Food Engineering* **2006,** *74*, 500-515.

[26] Souquet, J-L., Duclot, M. & Levy, M. Salt-polymer complexes: strong or weak electrolytes?. *Solid State Ionics* **1994**, *85*, 149-157.

[27] Bai, P., Li, J., Brushett, F. R., & Bazant, M. Z. Transition of lithium growth mechanisms in liquid electrolytes. *Energy Environ. Sci.* **2016**, *9*, 3221–3229.

[28] Sand, H. J. S. On the concentration at the electrodes in a solution, with special reference to the liberation of hydrogen by electrolysis of a mixture of copper sulphate and sulphuric acid. *Philos. Mag*. **1901,** *1*, 45–79.

[29] Tinevez, J-Y., et al. TrackMate: An open and extensible platform for single-particle tracking. *Methods* **2017,** *115*, 80-90.

2.5 Supporting Information

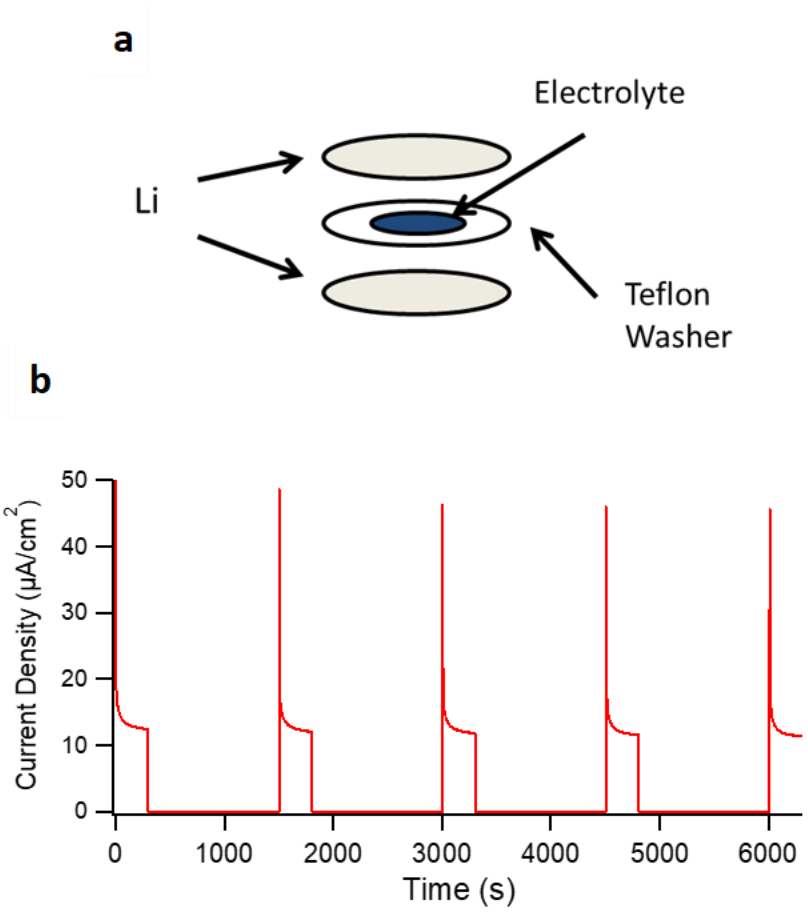

Figure 9: **a)** The electrochemical cell design to allow for free convection in the electrolyte. The symmetric lithium electrodes are separated by a 0.8mm Teflon washer that is filled with electrolyte. **b)** The current density as a function of time for the creation of current voltage curves. The current density at the end of each 5 minute voltage step was used to create the current voltage curves.

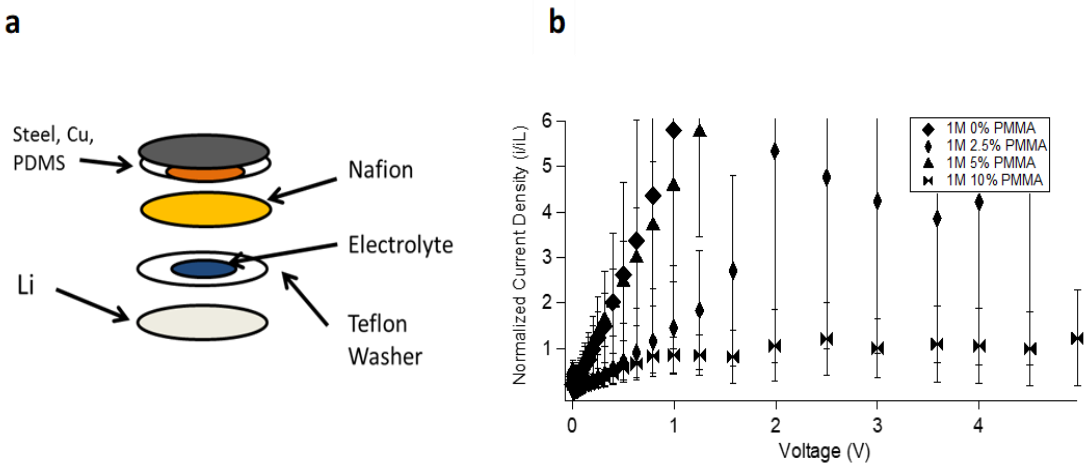

Figure 10: **a)** A new cell design that was used to test current voltage curves for an ion selective membrane. The cell design is very similar to the symmetric cell except a Nafion membrane is used in place of the rough lithium deposition. The top electrode was designed with a conductive copper center surrounded by PDMS to prevent growth of dendrites outside the confines of the washer **b)** The current voltage curve for the 1M LiTFSI electrolyte with the current normalized to either the experimental or theoretical (if no experimental could be determined) limiting currents. When compared to the 0.1M electrolyte a higher polymer concentration is needed to suppress the convection.

a

	Activation Energies (kJ/mol)	
PMMA Concentration	0.1M Electrolyte	1M Electrolyte
0%	2.70	2.77
2.50%	2.25	2.70
5%	2.90	3.49
10%	4.43	3.31

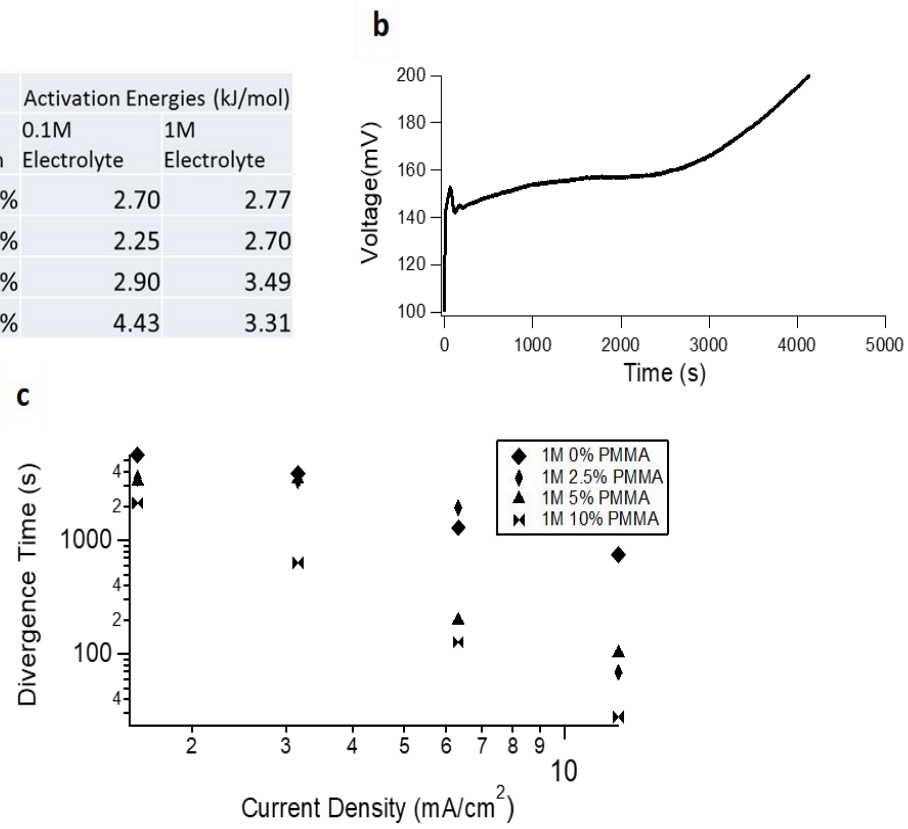

Figure 11: **a)** The resulting activation energies from fitting conductivity data with a VFT relationship. The activation energy remains relatively constant as polymer molecular weight changes. **b)** An example test for a constant current test where the voltage divergence occurs between 2000 and 3000 seconds. **c)** The divergence time as a function of current density for the 1M LiTFSI in EC/PC electrolyte.

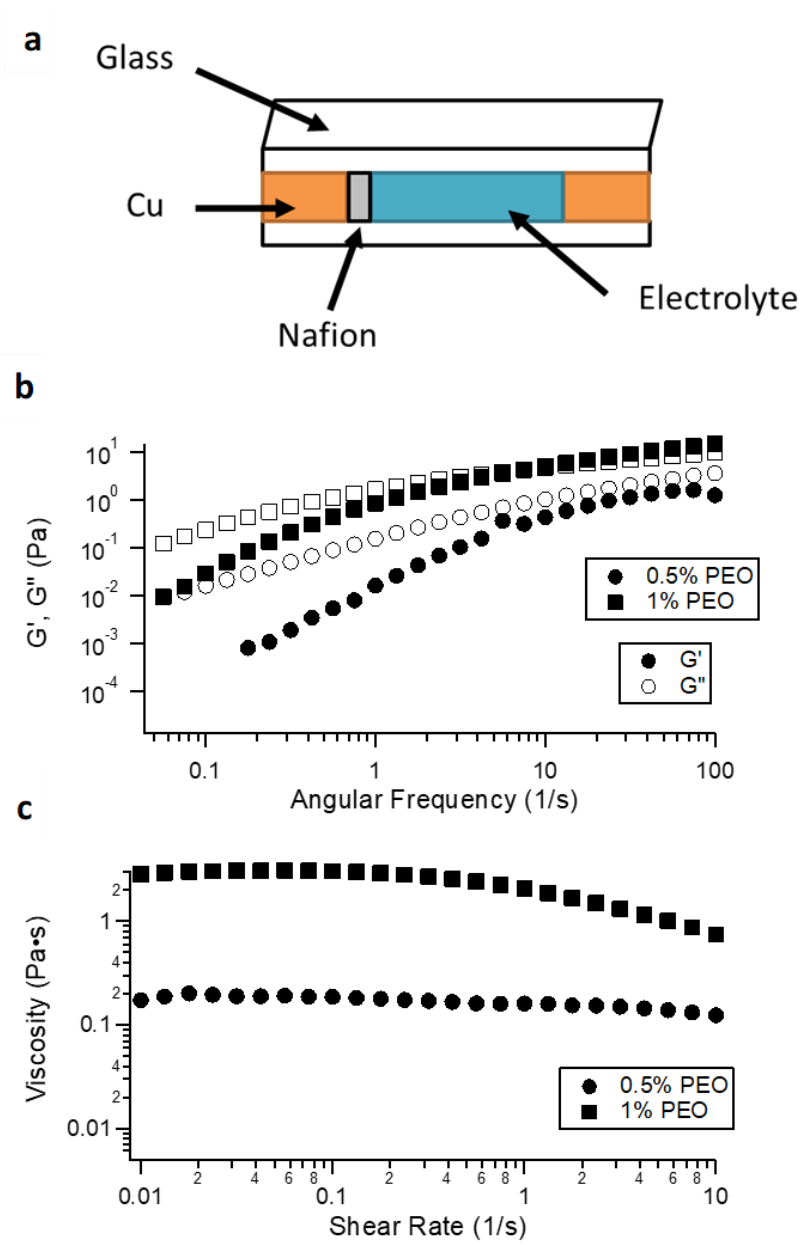

Figure 12: **a)** A visualization cell design that allowed for direct visualization of electroconvection. The microscope was focused onto the edge of the Nafion allowing for direct visualization of electroconvection. **b)** Frequency sweep rheological study (at 5°C to prevent solvent evaporation) for 0.01M $CuCl_{2\ (aq)}$ with two concentrations of Mw=8,000kg/mol PEO. The dependence of the storage (G') and loss (G'') moduli are plotted as a function of frequency. **c)** Shear rate sweep rheology of the same electrolytes demonstrating that as polymer concentration increases there is a transition from Newtonian behavior to non-Newtonian shear thinning.

Chapter 3: Dependence of Electroconvective Flow Structures on Voltage and Debye Length

3.1 Introduction

Electric field-driven transport of ions in an electrolyte bounded by at least one ion-selective planar interface (*e.g.*, the metal electrode in an electroplating process [1,2] or in a high-energy density battery[3] or the cation (or anion) selective membranes used for dialysis [4] or water desalination[5]), is conventionally thought to be limited by electroneutrality. In particular, when the ion depletion rate at the interface exceeds the rate of resupply from the bulk electrolyte, a diffusion limiting current, $i_L = \frac{4zcFD}{L}$is reached, wherein any additional flux of ions across the interface is resisted by a large electric field that preserves electroneutrality[6]. Here *c*, *z*, and *D* are the salt concentration, mobile ion valency, and diffusivity respectively; *L* the inter electrode spacing, and *F* is Faraday's constant. A significant body of early work showed that currents appreciably higher than i_L can be sustained by driving the operating potential in the cell to values substantially above the thermal voltage, $V_T = kT/e$ [7-9]. Complications associated with faradaic currents produced by redox chemistry of water initially prevented a full understanding of the origins of such *overlimiting* conductance [8, 10-11]. It is currently understood that the source of the behavior is the hydrodynamic instability termed *electroconvection*, an electro-osmotic flow driven by forces originating from coupling of the electric field and concentration polarization in electrolytes at ion-selective interfaces [12-14]. The resultant convective motions are thought to generate a mixing layer that enhances the ion transport beyond diffusion

limitations. These physics have been confirmed in experiments in which the overlimiting transport can be removed by immobilization of the diffusion layer [15].

Early theoretical studies show that electroconvection is formally the result of hydrodynamics produced when an extended space charge layer (ESCL), many times the length of the equilibrium double layer, forms at the ion-selective interface and couples to local electric fields to drive fluid motion. These arguments lead to a relationship between the thickness of the ESCL, ϵ, and both the relative voltage, $\hat{V} \equiv V/V_T$, and Debye screening length, $\hat{\delta} = \delta/L$: $\epsilon \approx L\ (\hat{V}\hat{\delta})^{2/3}$ [16]. It has more recently been shown by theoretical and direct numerical simulation studies that at voltages less than around 8 V_T electroconvection manifests as vortex structures that initiate at the ion-selective interface and ultimately grow into the inter-electrode space to enhance mixing within the electrolyte [17,18]. At much higher voltages, numerical simulations show further that the electroconvective flows become multiscale and chaotic [19,20].

Here we develop and use an in-situ particle tracking methodology to experimentally reveal how the structure of electroconvective flows near ion-selective interfaces evolve with variables such as electrolyte concentration and applied potential. Some experimental and simulation studies have focused on ways to control the electroconvection, either through imparting electrolyte viscoelasticity [21-23] or patterning the membrane surface [24]. A motivation for the present study is that better techniques may be developed with a more complete understanding of the flow. While experimental studies have shown the dependence of roll size and speed on the applied potential, an experimental understanding of the multiscale natures of these flows is yet to be explored [12, 25-27].

3.2 Results and Discussion

The main results reported in the letter are summarized in Figure 13. The figure reports gross features of the electroconvective flow generated in a dilute aqueous copper sulfate solution near an cation-selective, Nafion^{TM}, interface at large $\hat{V}$ values, using both vector maps (Fig. 13a, c) and in terms of profiles of the root mean squared component of the velocity (v) parallel to the electrode surface (Fig. 13b, d). The results in the latter figures capture at least three salient features of the electroconvection, which to our knowledge have not been experimentally studied. We outline these features first and discuss them in greater detail in the subsequent sections of the Letter. First, the RMS velocity distribution exhibits an initial maximum at a distance several tens of micrometers from the interface, *i.e.*, substantially larger than the equilibrium space charge thickness, ϵ. The size of the maximum is a strong increasing function $\hat{V}$; increasing nearly ten-fold for a four-fold increase in $\hat{V}$. Second, the RMS velocity decays slowly with distance from the interface, and a rather substantial convective flow is apparent even on length scales order 1mm from the ion-selective membrane surface. Finally, the flow is clearly structured, with a typically undulating velocity distribution. We note that the structuring becomes more distinct at higher values of $\hat{V}$. Comparisons with streamline plots and inspection of videos, reveal that the peaks in the v-component of the velocity correspond to the edges of different sized eddy structures; with the number of associated length scales changing from primarily two to three when $\hat{V}$ increases from approximately 78 to 315.

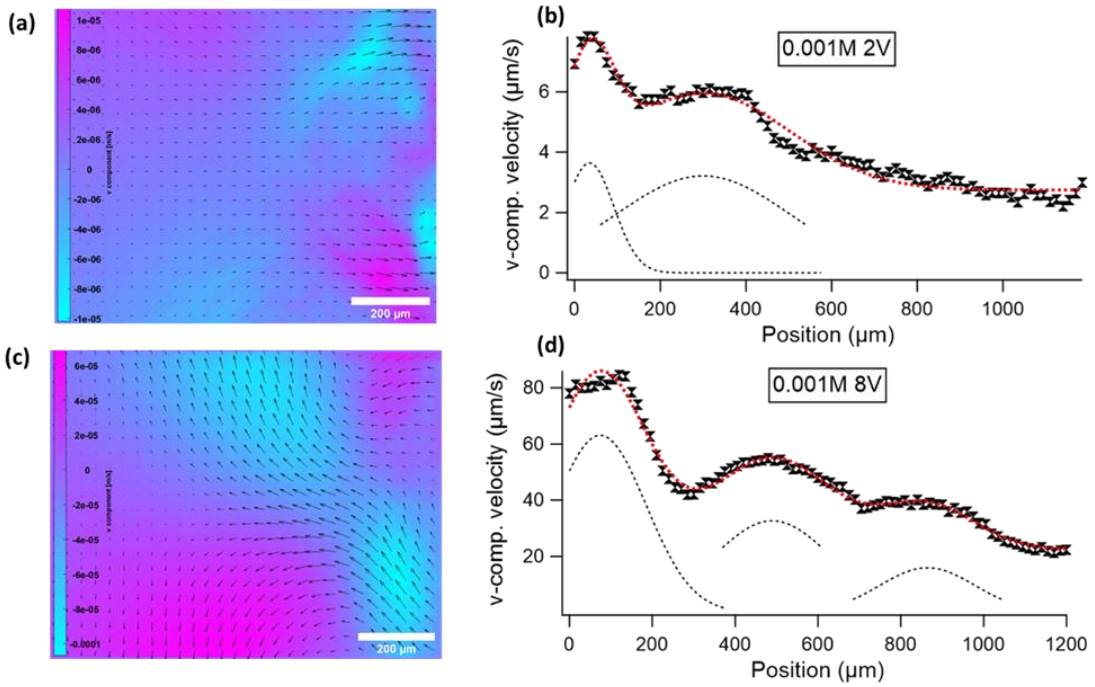

Figure 13: Effects of voltage on the electroconvective structures in 0.001M $CuSO_4$ $_{(aq)}$ electrolytes for a 2V (a), (b) and 8V (c), (d) potential difference across the cell. (a), (c) Vector maps with colors depicting the strength and sign of the velocity component parallel to the membrane (v-component). The Nafion membrane (x=0) is on the right side of these maps. (b), (d) Profiles of the root mean squared velocity component (v_{rms}) as a function of position.

The measurements reported in Figure 13 were obtained by first recording the motions of 3μm diameter spherical, colored polystyrene tracer particles using an Olympus BX51 optical microscope equipped with a CCD camera. Interfacing the microscope with the apparatus depicted in Figure 14 a, b enabled direct visualization of electroconvective flow in an aqueous $CuSO_4$ electrolyte as a function of distance from the edge of a Nafion-212 cation selective membrane. The zeta potential of the polystyrene tracer particles was measured using a Zeta sizer and found to be below 1mV for electrolyte

concentrations ranging from 0.1M-0.001M, and for a 0.1mM electrolyte the zeta potential is -5.6mV. We note that even at this higher zeta potential, the electrophoretic mobility measured in the same device is still about a factor of 7 or more lower than the peak velocity for the tracer component of the tracer particle velocity parallel to the electric field. Gravity is perpendicular to the electric field for the cell configuration used in the study, which reduces complications that could arise from Rayleigh-Bernard type convection arising from differences in Rayleigh numbers associated with concentration polarization [28,29]. The gap between the top and bottom glass plates was maintained fixed at 250μm to minimize 3-dimensional flow while still visualizing effects away from the surface of the glass cell boundaries [2]. The spacing between the Nafion and counter electrode supplying Cu^{+2} ions is 5mm, and the microscope has a viewing window of 1.3 x 1.3mm. The lowest electrolyte concentration used in the study was cut off at 0.1mM because independent ionic conductivity measurements revealed no change with salt concentration below this value. Videos obtained from the experiment were fed into the Particle Image Velocimetry software package (PIVLab) in Matlab, which uses cross-correlation to extract velocity vectors within the area of interest [30]. The frames used for the analysis were spaced 100ms apart and the final pass of each correlation yields a vector for each 15 x 15μm area. Although greater resolutions are possible, the associated lower signal: noise ratio obviated this choice.

Figure 14c reports a typical result of the particle path lines deduced from the measurements. The blue background represents the tracked vectors averaged over the last 40 seconds of a video taken at 6V in a 0.01M $CuSO_4$ electrolyte. Any background flow was removed by subtracting the average over each *x*-value. It is apparent that the

velocity vector distribution has components parallel to (v) as perpendicular (u) to the membrane surface. Figure 14d is the root mean squared average of u and v as a function of distance from the electrode. As with the v-component reported in Figure 13 at a lower salt concentration, the u-component also shows evidence of structuring of the electroconvective flow. The location of the peaks in v correlate well with the size of the convective eddies observed in the videos. For example, comparing Figure 14c and 14d, the peak at 100μm corresponds to the size of the small eddy (~150 μm) that is apparent in the vector plot. Likewise, the second peak in v at approximately 800 μm is close to the average size (~700 μm) of the second largest family of rolls observed in the video. In search of physical insights, in the following sections we analyze the measured velocity distributions over a range of applied potentials ($40 \leq \hat{V} \leq 320$) and electrolyte concentrations (0.1M – 0.1mM) to understand the effect $\hat{V}$ and δ on the electroconvective flow structure.

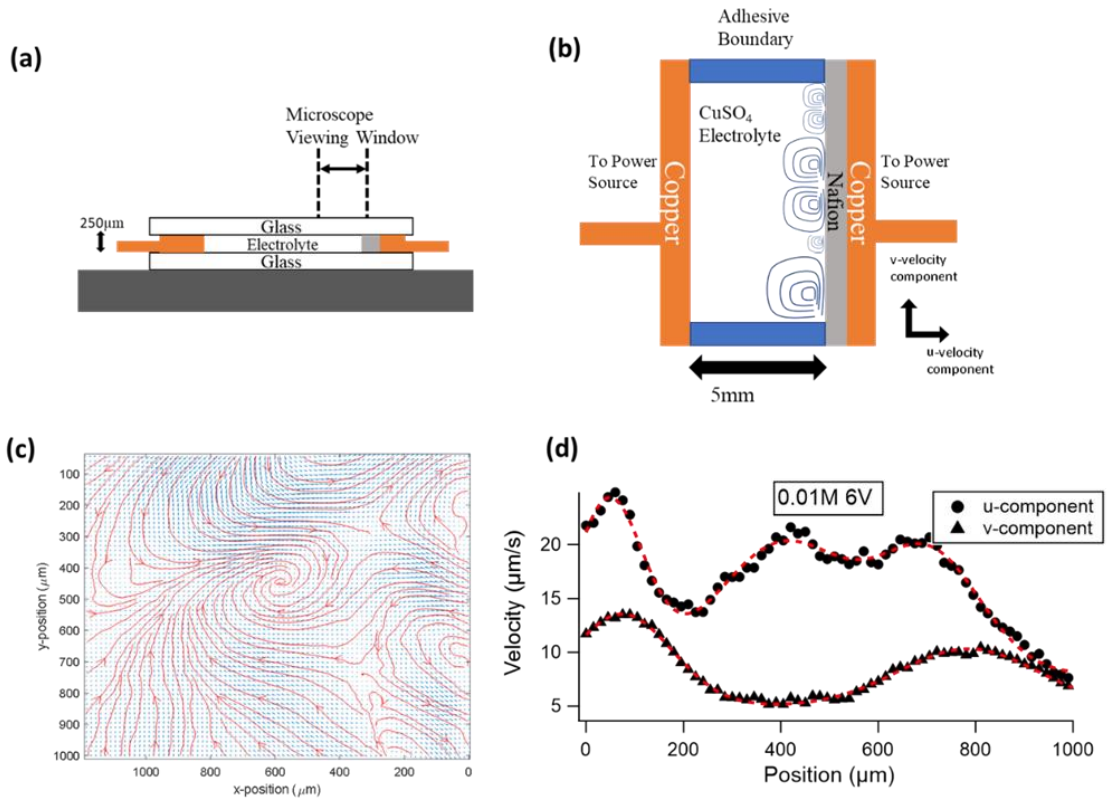

Figure 14: (a), (b) Depiction of the experimental cell used for visualizing convective flow. (c) Streamline of the flow for 0.01M $CuSO_4$ at a potential of 6V. (d) Profile of the root mean squared parallel (v_{rms}) and perpendicular (u_{rms}) velocity components for the same case as (c).

The first maximum in v is always characterized by the highest root mean squared velocity and its position coincides with the length scale of the smallest eddies observed in the corresponding video. Earlier numerical simulation studies also report a maximum in the tangential velocity component near ion-selective surface and associate the maximum with electroosmotic slip of fluid outside the ESCL and its location with the ESCL thicknesses ϵ [20]. At the conditions corresponding to Fig. 14d the ESCL thickness can be estimated, $\epsilon \approx 8.6$ μm; the corresponding values are $\epsilon \approx 9$ μm and $\epsilon \approx$ 22.5 μm for the results reported in Figs. 13b and 13d. It is therefore clear that the

experimentally determined first velocity maxima, v_{max}, are located at distances well outside the calculated range for ϵ, but as noted earlier, the location is consistent with the smallest eddy sizes detectable in the flow. We next study the effect of $\hat{V}$ on v_{max} in Figure 15a. It is seen that for $\hat{V} < 230$, v_{max} increases slightly stronger than linearly with $\hat{V}$, $v_{max} \sim \hat{V}^{1.1}$. This observation is consistent with results from numerical simulations which also show a linear relationship between voltage and the electroosmotic slip velocity [17]. An analogous relationship has been reported in earlier galvanostatic experiments in which the size of electroconvective vortices was found to scale approximately linearly with the applied current [12,25,26]. At higher potentials, a new regime occurs in which the voltage has a much stronger effect on the velocity as seen in the inset in Figure 15a. Experiments and simulations support the development of chaotic vortices at $\hat{V} > 50$ [19,20, 25], which could explain the increased convective flux at the largest $\hat{V}$ values used in the study.

A characteristic feature of electroconvection is that it develops gradually. Specifically, after imposition of a large-enough potential difference, *time* = 0 , the first sign of incipient convective motion is the appearance of eddies that form slowly, but accelerate as they extend into the bulk fluid, ultimately reaching a steady-state at intermediate $\hat{V}$ values. The acceleration rate is a strong function of $\hat{V}$. For example, in an electrolyte with 0.001M at $\hat{V} \approx 80$, the eddies take about 20 seconds to form and an additional 60 seconds or so to become fully developed. In contrast, for $\hat{V} \approx 320$, the eddies form within the first few seconds and extend into the bulk within 10 to 20 seconds. This last behavior is illustrated in the vector maps provided in Figure 13a, c where the direction

and strength of the flow is highly variable within the whole area of interest for $\hat{V} \approx 320$ but is more isolated and less variable in the $\hat{V} \approx 80$ scenario. At higher voltages the flow is more chaotic as eddies move along the membrane, collide, separate or even combine with each other to create structures that never appear to achieve a steady state. As pointed out previously, this transition to an unsteady, chaotic flow regime has also been reported in numerical simulations in which the chaotic nature of the flow creates concentration gradients throughout the electrolyte [20].

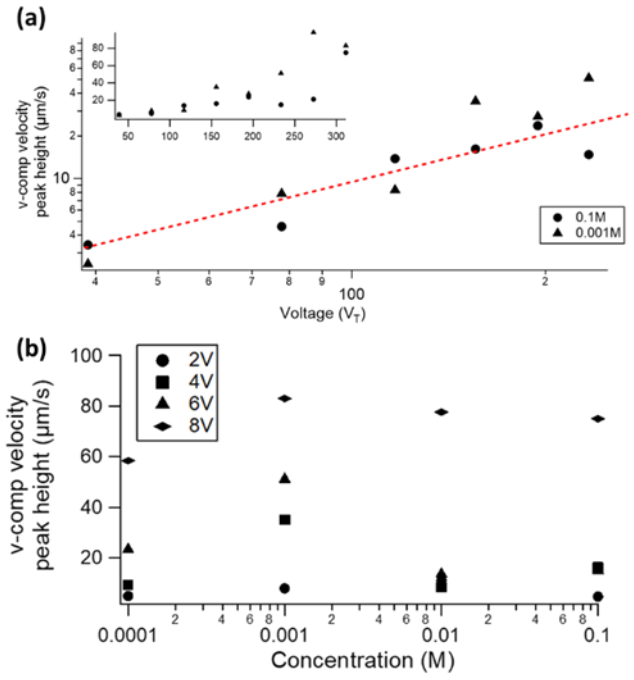

Figure 15: (a) Peak of the root mean squared v-component of velocity as a function of the applied potential. The dashed line depicts the scaling $V^{1.12}$. The inset shows that at higher potentials the effect of voltage is much stronger. (b) Peak of the root mean squared v-component of velocity as a function of the bulk electrolyte concentration for different applied potentials.

The Debye length δ scales with the bulk electrolyte concentration as $\delta \sim c^{-1/2}$, which at fixed potentials would yield a scaling relationship of the form, $\epsilon \sim c^{-1/3}$, between the ESCL thickness and electrolyte concentration. We created electrolytes with concentrations spanning 4 orders of magnitude, from 0.1M to 0.1mM, to evaluate this effect. Over this concentration range, δ is expected to increase from approximately 0.5nm to 15nm. Figure 15b reports the effect of *c* on v_{max} for various values of $\hat{V}$. It is seen that v_{max} is for all practical purposes is independent of *c* over the range of concentrations studied. Specifically, over a 4 order of magnitude change in concentration, v_{max} only deviates from the average by less than a factor of 2. Results reported in Figure 16 show that over this same concentration range, the eddy size distribution and structure of the electroconvective flow change markedly with *c*. For example, at a high salt concentration of 0.1M, the eddies remain small and localized near the ion-selective interface (Fig 16a, e). Additionally, irrespective of the $\hat{V}$ value, there is primarily only one velocity maximum observed at approximately 30 μm from the membrane surface for both components of the velocity. Looking further into the bulk there is a large reduction in convective motion, indicating that the convection is highly localized near the interface. As the concentration is reduced, additional peaks in both v and u emerge, suggesting more eddy sizes develop in the flow. This is confirmed as seen in the vector maps in Fig. 16 for the lower values of *c*. For the intermediate concentration range, 0.01M and 0.001M, the first peak velocity maximum is observed to move away from the membrane surface as the smallest convective roll propagates further into the bulk to distances ranging from 15-75μm. These high velocity eddies appear to bring more bulk solution to the interface, which increases the effective mixing.

Additionally, a second peak in v is apparent for these concentrations, confirming the multiscale nature of the flow. As the concentration is reduced even further to 0.1mM, the first velocity maximum again appears closer to the electrode and the second peak is still apparent. Notably, at $\hat{V} > 200$, a 3rd velocity maximum begins to appear in the 0.1mM electrolyte that causes the convective flow to reach further into the bulk, outside the viewing area of the microscope. The appearance of this 3rd maximum coincides with the transition to a chaotic state, resulting in additional complexity of the flow structure. The large scale of the convective eddy evident in Figure 16h may also suggest the presence of flow beyond the viewing window. Thus, while we are unable to confirm/disprove the $c^{-1/3}$ relationship between the location of the first maximum in v and ϵ suggested by numerical simulations, there is a clear inverse relationship between the structure, complexity, and reach of the electroconvective flow as the electrolyte concentration rises.

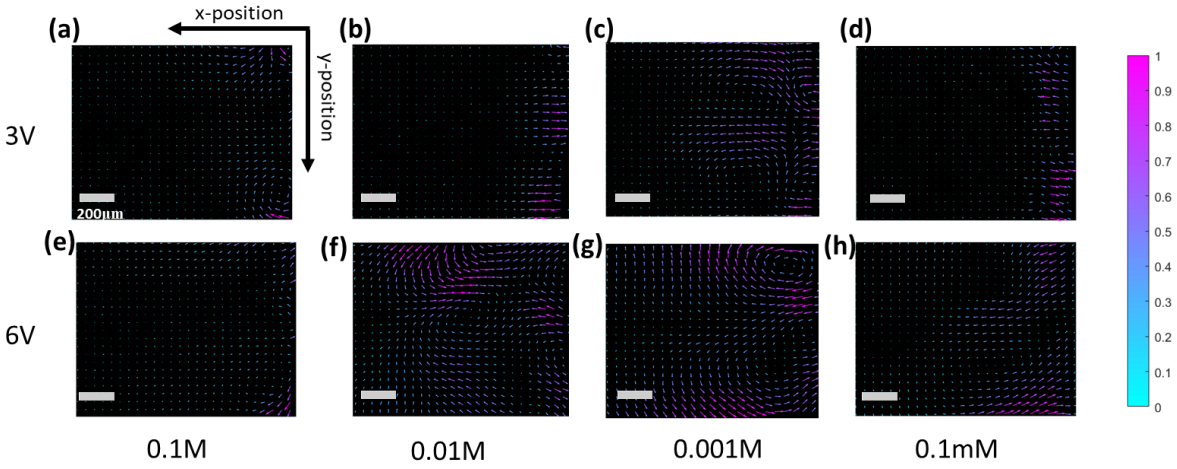

Figure 16: Vector maps of the flow for 3V polarization (a-d) and 6V polarization (e-h), at $CuSO_4$ concentrations of 0.1M (a,e), 0.01M (b,f), 0.001M (c,g), and 0.1mM (d,h). Each plots vectors size and color are non-dimensionalized by the maximum magnitude of that specific system. The bounds of the axis are 0 – 1,300μm in both x and y.

As is suggested with the coexistence of multiple peaks in the velocity profiles at low electrolyte concentration, there are multiple length scales in which the convection occurs. The electrolyte concentration appears to control the ratio of the small to large eddy sizes. For the intermediate concentrations, at all $\hat{V}$ values where v manifests at least two maxima, we compared the ratio of the position of these maxima to more quantitively assess the influence of ϵ on the structure of the electroconvective flow. For c = 0.001M the ratio is 7.35, whereas at c = 0.01M the ratio is 22.6; which can be crudely reduced to an approximate scaling of $c^{1/2}$ or $\hat{\delta}^{-1}$. This matches very closely to the results found via direct numerical simulations [31].

3.3 Conclusions

In summary we have visualized electroconvection at the surface of a cation-selective membrane for a range of electrolyte concentrations and applied potentials. Through particle tracking, vector fields of the videos were created to determine the effects of these properties. It is found that flow can occur simultaneously on multiple length scales near the surface. The effect of increasing potential is twofold, with both a velocity enhancement that scales just above linearly with applied potential, and an increase in flow chaos and complexity. The concentration does not have a significant impact on flow velocity but for lower concentrations additional eddy sizes extending into the bulk appear. The impact of electrolyte concentration is also realized in the ratio of small to larger eddy sizes which is a function of the dimensionless Debye length, scaling roughly as $\hat{\delta}^{-1}$.

3.4 References

[1] Fleury, V., Chazalviel, J. N., & Rosso, M. (1993). Coupling of drift, diffusion, and electroconvection, in the vicinity of growing electrodeposits. *Physical Review E*, *48*(2), 1279–1295. https://doi.org/10.1103/PhysRevE.48.1279

[2] Huth, J. M., Swinney, H. L., McCormick, W. D., Kuhn, A., & Argoul, F. (1995). Role of convection in thin-layer electrodeposition. *Physical Review E*, *51*(4), 3444–3458. https://doi.org/10.1103/PhysRevE.51.3444

[3] Tikekar, M. D., Choudhury, S., Tu, Z., & Archer, L. A. (2016). Design principles for electrolytes and interfaces for stable lithium-metal batteries. *Nature Energy*, *1*(9), 16114. https://doi.org/10.1038/nenergy.2016.114

[4] Urtenov, M. K., Uzdenova, A. M., Kovalenko, A. V., Nikonenko, V. V., Pismenskaya, N. D., Vasil'eva, V. I., Sistat, P., & Pourcelly, G. (2013). Basic mathematical model of overlimiting transfer enhanced by electroconvection in flow-through electrodialysis membrane cells. *Journal of Membrane Science*, *447*, 190–202. https://doi.org/10.1016/j.memsci.2013.07.033

[5] Nikonenko, V. V., Kovalenko, A. V., Urtenov, M. K., Pismenskaya, N. D., Han, J., Sistat, P., & Pourcelly, G. (2014). Desalination at overlimiting currents: State-of-the-art and perspectives. *Desalination*, *342*, 85–106. https://doi.org/10.1016/j.desal.2014.01.008

[6] Block, M., & Kitchener, J. A. (1966). Polarization Phenomena in Commercial Ion-Exchange Membranes. *Journal of The Electrochemical Society*, *113*(9), 947. https://doi.org/10.1149/1.2424162

[7] Seno, M., & Yamabe, T. (1963). Anomalous Conduction across Ion-exchange Membranes. *Bulletin of the Chemical Society of Japan*, *36*(7), 877–878. https://doi.org/10.1246/bcsj.36.877

[8] Fang, Y., Li, Q., & Green, M. E. (1982). Noise spectra of sodium and hydrogen ion transport at a cation membrane-solution interface. *Journal of Colloid And Interface Science*, *88*(1), 214–220. https://doi.org/10.1016/0021-9797(82)90167-9

[9] Yafuso, M., & Green, M. E. (1971). Noise spectra associated with hydrochloric acid transport through some cation-exchange membranes. *Journal of Physical Chemistry*, *75*(5), 654–662. https://doi.org/10.1021/j100675a010

[10] Frilette, V. J. (1957). Electrogravitational transport at synthetic ion exchange membrane surfaces. *Journal of Physical Chemistry*, *61*(2), 168–174. https://doi.org/10.1021/j150548a010

[11] Lifson, S., Gavish, B., & Reich, S. (1978). Flicker noise of ion-selective membranes and turbulent convection in the depleted layer. *Biophysics of Structure and Mechanism*, *4*(1), 53–65. https://doi.org/10.1007/BF00538840

[12] Rubinstein, S. M., Manukyan, G., Staicu, A., Rubinstein, I., Zaltzman, B., Lammertink, R. G. H., Mugele, F., & Wessling, M. (2008). Direct observation of a nonequilibrium electro-osmotic instability. *Physical Review Letters*, *101*(23), 236101. https://doi.org/10.1103/PhysRevLett.101.236101

[13] Zaltzman, B., & Rubinstein, I. (2007). Electro-osmotic slip and electroconvective instability. *Journal of Fluid Mechanics*, *579*, 173–226.

https://doi.org/10.1017/S0022112007004880

[14] Rubinstein, I., & Zaltzman, B. (2000). Electro-osmotically induced convection at a permselective membrane. *Physical Review E - Statistical Physics, Plasmas, Fluids, and Related Interdisciplinary Topics*, *62*(2), 2238–2251. https://doi.org/10.1103/PhysRevE.62.2238

[15] Maletzki, F., Rösler, H. W., & Staude, E. (1992). Ion transfer across electrodialysis membranes in the overlimiting current range: stationary voltage current characteristics and current noise power spectra under different conditions of free convection. *Journal of Membrane Science*, *71*(1–2), 105–116. https://doi.org/10.1016/0376-7388(92)85010-G

[16] Rubinstein, I., Zaltzman, B., & Lerman, I. (2005). Electroconvective instability in concentration polarization and nonequilibrium electro-osmotic slip. *Physical Review E - Statistical, Nonlinear, and Soft Matter Physics*, *72*(1). https://doi.org/10.1103/PhysRevE.72.011505

[17] Druzgalski, C. L., Andersen, M. B., & Mani, A. (2013). Direct numerical simulation of electroconvective instability and hydrodynamic chaos near an ion-selective surface. *Physics of Fluids*, *25*(11), 110804. https://doi.org/10.1063/1.4818995

[18] Demekhin, E. A., Nikitin, N. V., & Shelistov, V. S. (2013). Direct numerical simulation of electrokinetic instability and transition to chaotic motion. *Physics of Fluids*, *25*(12). https://doi.org/10.1063/1.4843095

[19] Davidson, S. M., Andersen, M. B., & Mani, A. (2013). Chaotic induced-charge electro-osmosis. *Physical Review Letters*, *112*(12), 1–5.

https://doi.org/10.1103/PhysRevLett.112.128302

[20] Druzgalski, C., & Mani, A. (2016). Statistical analysis of electroconvection near an ion-selective membrane in the highly chaotic regime. *Physical Review Fluids*, *1*(7), 073601. https://doi.org/10.1103/PhysRevFluids.1.073601

[21] Li, G., Archer, L. A., & Koch, D. L. (2019). Electroconvection in a Viscoelastic Electrolyte. *Physical Review Letters*, *122*(12), 124501. https://doi.org/10.1103/PhysRevLett.122.124501

[22] Warren, A., Zhang, D., Choudhury, S., & Archer, L. A. (2019). Electrokinetics in viscoelastic liquid electrolytes above the diffusion limit. *Macromolecules*, *52*(12), 4666–4672. https://doi.org/10.1021/acs.macromol.9b00536

[23] Zhang, D., Warren, A. J., Li, G., Cheng, Z., Han, X., Zhao, Q., Liu, X., Deng, Y., & Archer, L. A. (2020). Electrodeposition of Zinc in Aqueous Electrolytes Containing High Molecular Weight Polymers. *Macromolecules*. https://doi.org/10.1021/acs.macromol.0c00037

[24] Davidson, S. M., Wessling, M., & Mani, A. (2016). On the Dynamical Regimes of Pattern-Accelerated Electroconvection. *Nature Publishing Group*, *March*, 1–10. https://doi.org/10.1038/srep22505

[25] De Valença, J. C., Wagterveld, R. M., Lammertink, R. G. H., & Tsai, P. A. (2015). Dynamics of microvortices induced by ion concentration polarization. *Physical Review E - Statistical, Nonlinear, and Soft Matter Physics*, *92*(3), 031003. https://doi.org/10.1103/PhysRevE.92.031003

[26] Kwak, R., Guan, G., Peng, W. K., & Han, J. (2013). Microscale electrodialysis: Concentration profiling and vortex visualization. *Desalination*, *308*, 138–146.

https://doi.org/10.1016/j.desal.2012.07.017

[27] Yossifon, G., & Chang, H. C. (2008). Selection of nonequilibrium overlimiting currents: Universal depletion layer formation dynamics and vortex instability. *Physical Review Letters*, *101*(25), 254501. https://doi.org/10.1103/PhysRevLett.101.254501

[28] Karatay, E., Andersen, M. B., Wessling, M., & Mani, A. (2016). Coupling between Buoyancy Forces and Electroconvective Instability near Ion-Selective Surfaces. *Physical Review Letters*, *116*(19), 33–37. https://doi.org/10.1103/PhysRevLett.116.194501

[29] De Valença, J. C., Kurniawan, A., Wagterveld, R. M., Wood, J. A., & Lammertink, R. G. H. (2017). Influence of Rayleigh-Bénard convection on electrokinetic instability in overlimiting current conditions. *Physical Review Fluids*, *2*(3), 033701. https://doi.org/10.1103/PhysRevFluids.2.033701

[30] Thielicke, W., & Stamhuis, E. J. (2014). PIVlab – Towards User-friendly, Affordable and Accurate Digital Particle Image Velocimetry in MATLAB. *Journal of Open Research Software*, *2*(1). https://doi.org/10.5334/jors.bl

[31] Wang, K., & Mani, A. (2018). Scale dependence of flow structures in electroconvection. *Bulletin of the American Physical Society*, *Volume 63, Number 13*.

3.5 Supporting Information

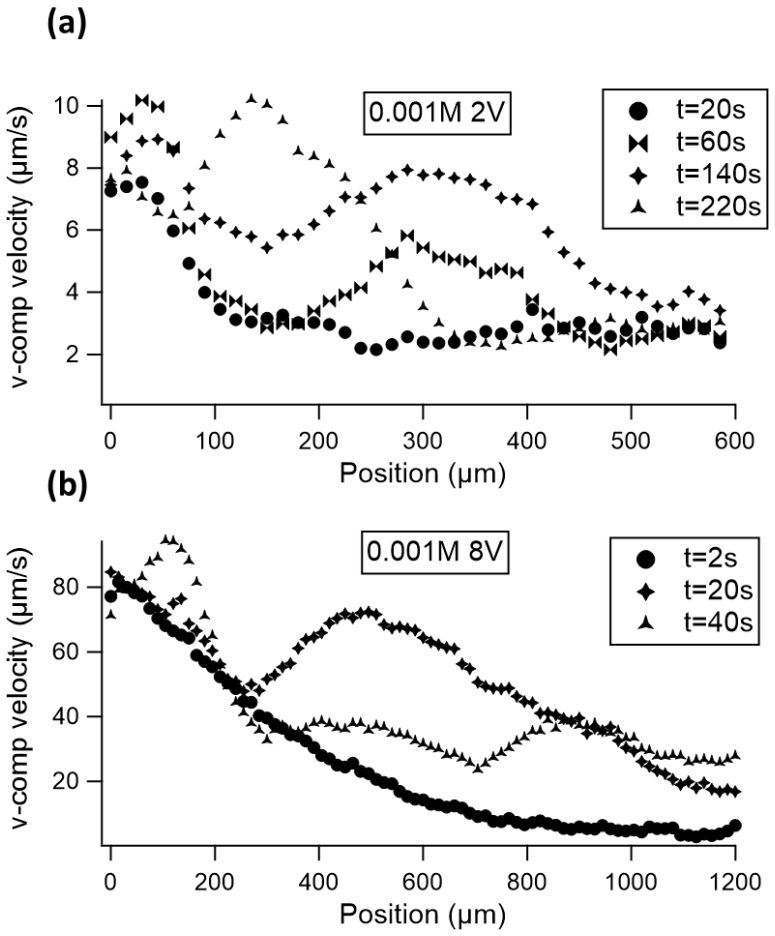

Figure 17: Effects of time on the electroconvection structure shown via profiles of the root mean squared velocity component (v_{rms}) as a function of position for an electrolyte concentration of 0.001M $CuSO_4$. (a) Profiles for an applied potential of 2V at t= 20s, 60s, 140s and 220s. The second peak location shifts outward and the velocity grows during the first 2 minutes, until it sets back closer to the membrane for longer times. (b) Profiles for an applied potential of 8V at t= 2s, 20s, and 40s. In comparison to the 2V the peaks set in much faster for the 8V potential. Over time more peaks form and within 1 minute a 3rd peak forms demonstrating the more complex structure of this flow.

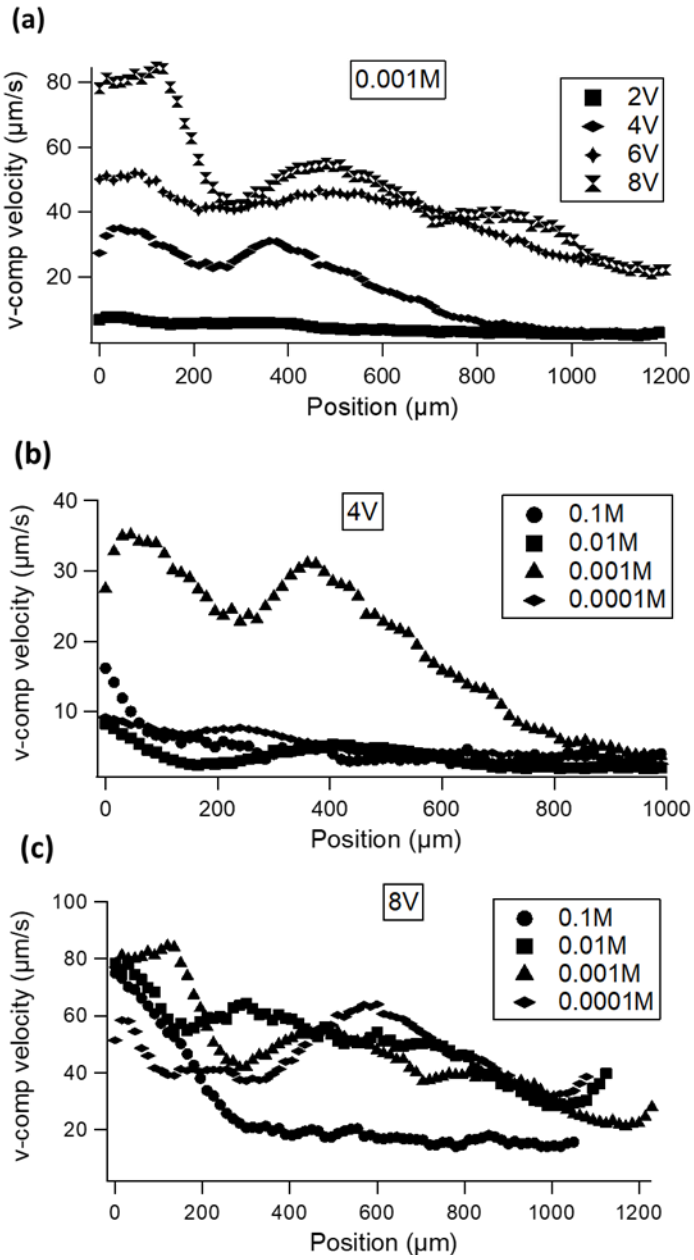

Figure 18: (a) Profiles of the root mean squared v-component of velocity for 0.001M $CuSO_4$ for applied potentials of 2V, 4V, 6V and 8V. The peak velocity can be seen to be increasing as a function of the applied potential. (b) Profiles of the root mean squared v-component of velocity for an applied potential of 4V at concentrations ranging from 0.1M – 0.1mM. Other than the velocity enhancement in 0.001M the concentration does not have a significant impact. (c) Profiles of the root mean squared v-component of velocity for an applied potential of 8V at concentrations ranging from 0.1M – 0.1mM. The concentration does not have a significant impact on the velocity but there is an increase in number length scales present at the concentration is reduced.